Journal of Materials Chemistry A

Nanocomposite Electrodes as a New Opportunity to Transform the Performance of Solid Oxide Cells

Journal:	*Journal of Materials Chemistry A*
Manuscript ID	TA-REV-09-2023-005430.R1
Article Type:	Review Article
Date Submitted by the Author:	13-Nov-2023
Complete List of Authors:	Li, Xuemei; West Virginia University, Department of Chemical and Biomedical Engineering Zhou, Lingfeng; West Virginia University College of Engineering and Mineral Resources, Department of Chemical and Biomedical Engineering Li, Qingyuan; West Virginia University, Department of Mechanical and Aerospace Engineering Kalu, Awa; West Virginia University College of Engineering and Mineral Resources, Department of Chemical and Biomedical Engineering Liu, Cijie; West Virginia University Guan, Bo ; National Energy Technology Laboratory Morgantown Molouk, Ahmed Fathi Salem; Mansoura University Faculty of Science, Chemistry Liu, Xingbo; West Virginia University, Department of Mechanical and Aerospace Engineering Li, Wenyuan; West Virginia University College of Engineering and Mineral Resources, Department of Chemical and Biomedical Engineering

Nanocomposite Electrodes as a New Opportunity to Transform the Performance of Solid Oxide Cells

Xuemei Li[a], Lingfeng Zhou[a], Qingyuan Li[b], Awa Kalu[a], Cijie Liu[b], Bo Guan[c], Ahmed Fathi Salem Molouk[d], Xingbo Liu[b, *], Wenyuan Li[a,*]

[a] *Chemical and Biomedical Engineering Department, West Virginia University, Morgantown, West Virginia, USA*

[b] *Mechanical & Aerospace Engineering Department, West Virginia University, Morgantown, West Virginia, USA*

[c] *DOE National Energy Technology Laboratory, 3610 Collins Ferry Road, Morgantown, West Virginia, USA*

[d] *Chemistry Department, Faculty of Science, Mansoura University, Mansoura, Egypt*

* Corresponding author: xingbo.liu@mail.wvu.edu, wenyuan.li@mail.wvu.edu

Abstract

Solid Oxide Cells (SOCs) are poised to serve as economically vital, high-efficiency energy conversion devices. But certain critical issues persist in their current stage of development, including system aging during high temperature operation, or reduced performance at low temperature running. To tackle these challenges and drive the advancement of SOC technology, nanocomposite electrodes have emerged as a promising and revolutionary solution to provide high performance and durability at the same time. Persistent efforts have been dedicated to the development of novel nanocomposite electrodes and unraveling the underlying working mechanisms of nanostructured heterogeneous electrodes. These advancements are fueled by the remarkable enhancements that nanocomposites offer, not only in terms of ionic and/or electronic conductivity but also in electrocatalytic activity and stability for SOC. Both experimental results and theoretical calculations validate these enhancements, making nanocomposites an attractive avenue for exploration. To summarize the recent advancements and provide a forward-looking insight regarding this field in this review, we (1) start with an overview of the progress in the development of nano-scaled composite electrodes, encompassing both oxygen ion conducting and proton conducting systems, (2) then highlight the unique attributes of nanocomposite electrodes in the enhancement of the SOC performance, (3) delve into the various techniques used to fabricate nanocomposite electrodes with precise control over their composition, structure, and morphology, and (4) finally acknowledge these remaining obstacles and take a critical look at the hurdles that need to be overcome. Alongside identifying these challenges, we propose potential strategies and research directions to address them effectively. By

bridging the gap between current research progress and future possibilities, we aspire to inspire further exploration and innovation in electrochemical energy conversion systems.

1. Introduction

SOCs are a class of energy conversion devices that operate at temperatures 500~900°C. They employ a solid electrolyte to facilitate the conduction of oxygen ions or protons, encompassing two types: solid oxide fuel cells (SOFCs) and solid oxide electrolyze cells (SOECs)[1]. The inherent advantages of SOCs, including their high efficiency, fuel flexibility, and potential for low emissions, have attracted considerable attention, positioning them as promising candidates for achieving a low-carbon or even zero-carbon economy[2-5].

Despite the numerous advantages and broad application prospects of SOC systems, their large-scale implementation faces a significant hurdle in the form of high operating temperatures. Although such elevated temperatures enhance reaction kinetics and ionic conductivity, they also promote unfavorable interactions among cell components, resulting in reduced durability and heightened utilization costs[6]. To overcome these challenges and develop more efficient, durable, and economically viable SOC systems, it is imperative to lower the operating temperature to approximately 500°C while ensuring a sufficiently high level of performance[7-10]. However, reducing the operating temperature comes with its own set of challenges. As the temperature decreases, the cell's performance experiences an exponential decline due to the sluggish oxygen reduction/evolution (ORR/OER) reaction kinetics on the oxygen electrode and increased polarization resistance of the fuel electrode[11-14]. To tackle this issue, innovative materials and novel structures for SOC electrodes must be designed to facilitate high electrocatalytic activity and durability under the operating conditions. In recent years, nanocomposites have emerged as promising materials for SOC applications[7, 15, 16]. Electrodes made of nanocomposites have garnered significant attention due to their exceptional electrocatalytic activity at relatively low temperatures, their abundant electron/ionic reaction sites at the heterointerface, and their enhanced stability, making them a compelling option for advancing SOC technology.

One critical challenge associated with SOCs relates to the sluggish kinetics observed at the electrode-electrolyte interfaces, such as ORR/OER and fuel oxidation reactions. These slow reaction rates contribute to significant polarization losses[17]. To over the drawback, various advanced materials before nanocomposites have been developed. In the conventional air electrodes, various studies focus on the perovskite-related multi-conducting oxide families, including three main types as potential low-temperature

SOC air electrode: cubic-type perovskites (ABO_3), layered perovskites ($AA'B_2O_6$), and the Ruddlesden-Popper (RP) $A_{n+1}B_nO_{3n+1}$ phases[18-20]. Currently, the majority of air electrode materials for SOCs include Sr-doped $LaCoO_{3-\delta}$ (LSC), Sr-doped $LaFeO_{3-\delta}$ (LSF), $Sm_{0.5}Sr_{0.5}CoO_{3-\delta}$ (SSC), $Ba_{0.5}Sr_{0.5}Co_{0.8}Fe_{0.2}O_{3-\delta}$ (BSCF), and Sr-doped $La_{0.6}Sr_{0.4}Co_{0.2}Fe_{0.8}O_{3-\delta}$ (LSCF)[21, 22]. These materials exhibit good catalytic activity for electrochemical reactions, especially for the ORR/OER, within a wide temperature range of 500-800°C[23-26]. However, the conventional single-phase electrodes based on perovskite materials have still fallen short of meeting the demanding requirements of SOC systems due to various challenges. These include microstructural coarsening, thermal mismatching, cation surface segregation, interfacial reactions, and susceptibility to deposition and poisoning by volatile impurities like CrO_3, SO_2, BO_2, CO_2, and H_2O within SOC stacks[27].

To address these limitations, researchers have explored the potential of heterointerfaces in composite electrodes to significantly enhance the performance of SOC electrodes. Experimental findings and theoretical calculations have demonstrated that incorporating heterointerfaces can lead to improved ionic and/or electronic conductivity, enhanced electrocatalytic activity, and better electrode stability in SOC systems[28-31]. For instance, Crumlin et al. utilized pulsed laser deposition (PLD) to decorate (La, Sr)CoO_3 thin films with epitaxially grown (La, Sr)$_2CoO_4$, resulting in a substantial 1–3 orders of magnitude enhancement in the ORR activity[32]. Additionally, Sun et al. reported remarkable achievements with $La_{0.3}Sr_{0.6}Ce_{0.1}Ni_{0.1}Ti_{0.9}O_{3-\delta}$ (LSCNT) fuel electrodes containing Ni–Ce exsoluted particles. These electrodes exhibited outstanding activities, reaching a peak power density of 600 mW cm^{-2}, and demonstrated exceptional resistance to coking for more than 80 hours in a CH_4 atmosphere[33]. These encouraging results highlight the promising potential of heterointerfaces and composite electrode materials in overcoming the limitations of conventional single-phase electrodes, bringing us closer to realizing highly efficient and stable SOC systems. Previous investigations on the electrode-electrolyte composite air electrode have identified the microstructure as crucial for achieving optimal performance[34, 35]. In this context, nanocomposite electrodes have garnered significant attention due to their potential to extend the length of the triple-phase boundary (TPB) and offer numerous interfacial active sites for electrochemical processes[36]. This review paper aims to provide an in-depth analysis of the potential of nanocomposite electrodes as a gamechanger in the field of SOCs. By exploring the application of nanocomposites in air and fuel electrodes, the review aims to shed light on their unique properties and advantages over conventional electrode

materials. The incorporation of nanoscale catalysts to improve the oxygen reduction kinetics and enhance the overall performance of SOCs, and the utilization of nanoscale fuel electrode materials to enhance the fuel oxidation kinetics and mitigate carbon deposition are discussed in detail. The unique nature of nanocomposite electrodes, which collectively contribute to the superior electrochemical performance is comprehensively discussed. Additionally, various techniques and strategies employed to construct nanocomposite electrodes are presented. These insights would provide a comprehensive understanding of the fabrication and optimization of nanocomposite electrodes for enhanced SOC performance.

2. Application of nanocomposite electrodes

2.1 Basic concept of nanocomposite

Nanocomposites, as the name suggests, refer to materials composed of two or more distinct components at the nanoscale. In the context of SOCs, nanocomposites play a significant role in improving the performance of electrodes. These nanocomposite electrodes typically consist of a combination of materials with different functionalities, such as catalysts, conductors, and stabilizers. The integration of these components at the nanoscale facilitates shorter paths for charge/mass transfer and provides a larger surface area for reactions, which confers several notable advantages, including heightened catalytic activity, enhanced electronic and ionic conduction, and greater stability.

2.2 Nanocomposites in air electrodes

Air electrodes play a crucial role in SOCs as they are responsible for facilitating the OER and ORR during cell operation. These electrochemical catalytic reactions in SOCs differ significantly from normal heterogeneous catalytic reactions. The OER and ORR involve several steps, including oxygen gas diffusion, oxygen adsorption, dissociation, electron transfer, as well as the diffusion of oxygen ions on the surface or within the bulk, and cross-transfer of oxygen ions at the electrode/electrolyte interface. The interfaces between different phases in nanocomposites provide enhanced pathways for electronic and ionic conduction. These interfaces facilitate the efficient transport of charge carriers, reducing the ohmic losses and enhancing the overall conductivity of the electrode. This section explores the implementation of nanocomposite air electrodes in oxygen-conducting and proton-conducting systems.

2.2.1 Nanocomposite for oxygen-conducting system

Numerous research groups have made significant strides in developing intricate nanocomposite air electrodes within oxygen-conducting systems, employing a range of straightforward synthesis methods.

From multiphase perovskite oxide composites obtained by spray pyrolysis to vertically aligned nanocomposites woven by sputtering, and to composites with different stoichiometry and composition synthesized by one-pot pechini self-assembly, the advancements have consistently demonstrated impressive electrocatalytic reactivity and exceptional stability, whether applied in fuel cell or electrolysis modes. In this section, we offer a comprehensive summary of the performance and distinctive characteristics exhibited by these cutting-edge structural materials.

Nanocomposite electrode investigation can be dated back to $La_{0.8}Sr_{0.2}MnO_{3-\delta}$ (LSM) air electrode. Though conventional LSM air electrode material stands out due to its cost-effectiveness and compatibility with the YSZ electrolyte at a physical and chemical level, it exhibits low ionic conductivity, which hampers the electrochemical reactions occurring at the TPB sites, primarily due to its poor catalytic activity for the oxygen reduction reaction at temperatures below 800 ^{o}C[37]. To address this limitation, Shimada et al. successfully developed a microstructure-controlled air electrode by utilizing a nano-composite powder comprising LSM and $Ce_{0.8}Gd_{0.2}O_{1.9}$ (GDC), synthesized through spray pyrolysis (**Fig. 1a-b**)[38]. This type of nanocomposite electrodes demonstrated exceptional performance in steam electrolysis operations and maintained stable functionality without any degradation in both continuous SOEC and SOFC-SOEC operations (**Fig. 1c**).

SSC is another electrode material that exhibits both electronic and ionic conductivity. Shimada et al. designed nanocomposite electrodes through spray pyrolysis, starting from raw powder materials[15]. These electrodes consisted of SSC as a perovskite oxide and $Ce_{0.8}Sm_{0.2}O_{1.9}$ (SDC) as a fluorite oxide. The resulting nanocomposite electrodes exhibited excellent cell performance. A bimodal structure, where nanometer-scale SSC and SDC extended the TPB region, was observed, and both electronic and ionic conductive networks were formed with broad pore channels within the sub-micrometer-scale particles (**Fig. 1d-f**). The solid oxide electrolysis cells utilizing these nanocomposite electrodes demonstrated impressive current densities during steam electrolysis operations (**Fig. 1g**). At 750 °C, the cells achieved a high current density of 3.13 A cm^{-2} at 1.3 V, and 4.08 A cm^{-2} at 800 ^{o}C. These current densities corresponded to hydrogen production rates of 1.31 and 1.71 L h^{-1} cm^{-2}, respectively.

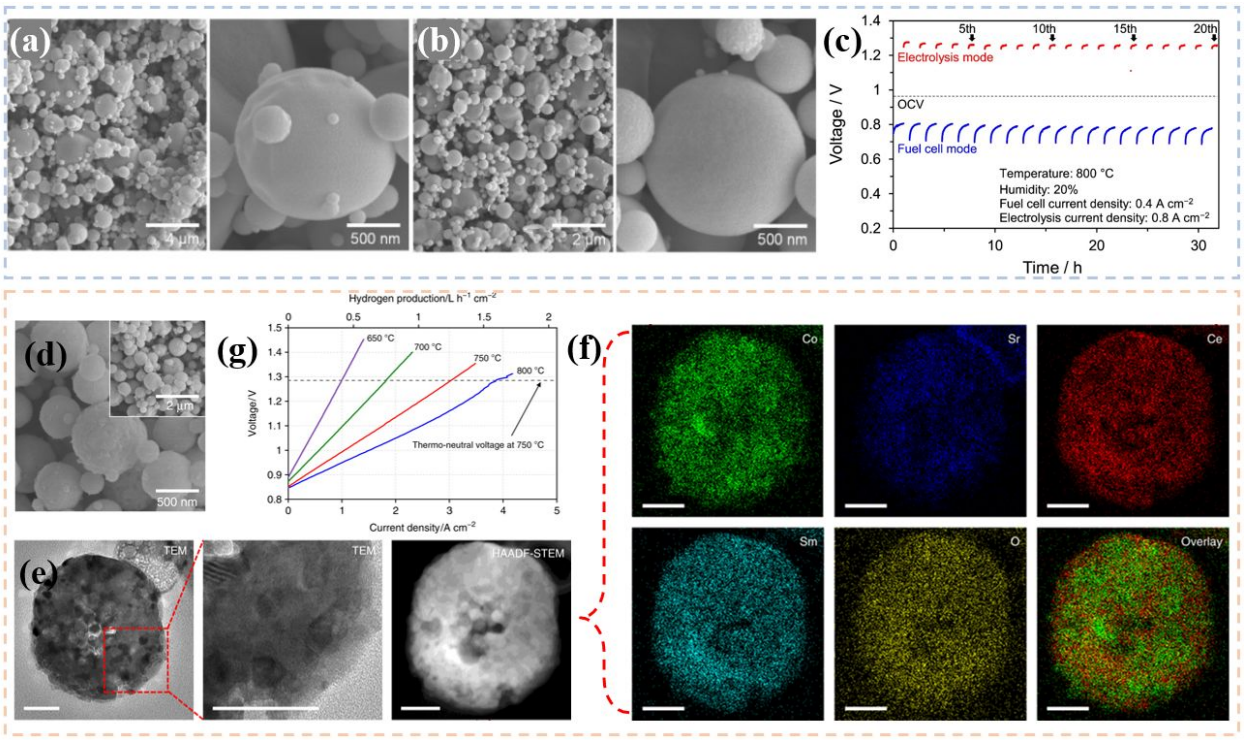

Fig. 1 FE-SEM images and particle size distribution of as-prepared LSM-GDC nanocomposite particles synthesized by spray pyrolysis: (a) LS64M-GDC and (b) LS46M-GDC nanocomposite particles, and (c) Durability in reversible SOFC-SOEC cyclic operation for SOC with LS46M-GDC nanocomposite electrode at 800 °C under 20% humidity condition[38]. Copyright 2020, Ceramic International. (d) Characterization of nanocomposite particles prepared by spray pyrolysis. a FE-SEM images of a representative SSC-SDC(50:50) nanocomposite particles, (e) TEM and HAADF-STEM images, (f) EDX mappings of Co, Sr, Ce, Sm, and O of a representative SSC-SDC(50:50) nanocomposite particle. Overlay image of Co and Ce mapping is also shown. Scale bars in c and d indicate 100 nm, and (g) a I–V characteristics and corresponding hydrogen production for the SOEC at 650–800 °C under 50% humidity condition[15]. Copyright 2019, Nature Communications.

While YSZ is widely used as an electrolyte material in SOCs, the formation of secondary insulating chemical phases, such as $La_2Zr_2O_7$ (LZO) and $SrZrO_3$ (SZO), at higher temperatures poses limitations on the performance of composite materials like LSM/YSZ and LSF/YSZ. Additionally, at lower operating temperatures, the sluggish oxygen surface kinetics at the YSZ electrolyte surface further hinders SOFC performance[39]. To overcome these challenges, numerous studies have focused on combining LSM with various ionic conductors, including GDC, Sc_2O_3-stabilized-ZrO_2 (SSZ) and $Bi_{1.5}Y_{0.5}O_{3-\delta}$ (BYO).

Hagiwara et al. developed LSM + SSZ electrolyte/electrode nanocomposite air electrodes using "pre-fabricated" powder synthesized through spray pyrolysis[40]. They discovered the importance of self-structure behavior during air electrode fabrication to achieve precise control of the air electrode microstructure. The grains of the electrolyte establish connections with other electrolyte grains, forming a main-frame

electrolyte network. As the heat treatment progresses, the crystal size of the composite phases increases without significant secondary phase formation, resulting in improved performance due to a narrow particle size distribution.

Further, LSC, SSC, or BSCF materials which exhibit significantly higher catalytic activity than LSM at intermediate temperatures displayed tremendous potential in nanocomposite electrode. LSC, in particular, is a promising candidate for air electrode material, especially in intermediate temperature SOCs (500-700 ^{o}C)[41]. It has been reported that combining LSC with rare-earth-doped ceria, such as GDC, in a composite structure leads to superior air electrode performance, including extremely low polarization resistances even at lower temperatures, benefiting from heterointerfaces and an increased number of TPBs[42, 43]. Ren et al. reported on a porous nanostructured ceramic air electrode composed of gadolinium-cerium (Gd-Ce) alloy and LSC perovskite targets, obtained through magnetron co-sputtering (**Fig. 2a-c**). Thin-film cells based on YSZ electrolyte exhibited high performance, achieving peak power densities (PPD) of 0.14, 0.48, 1.21, 2.56, and 3.01 W cm^{-2} at 450, 500, 550, 600, and 650 °C, respectively (**Fig. 2d**)[43].

LSCF is a commonly used air electrode material known for its high ionic and electronic conductivity, which allows for the extension of active sites beyond the TPBs. By integrating nanoengineering air electrode layers into conventional fuel electrode-supported cells, the electrochemical performance can be significantly enhanced. Develos-Bagarinao et al. made an innovative development by creating an fuel electrode-supported high-performance nanoengineered air electrode[44]. This air electrode comprised a nano-porous LSC thin film with self-assembled and highly ordered LSCF-GDC nanocomposites (**Fig. 2e-k**). The combination of these two layers resulted in superior air electrode performance with remarkably low ASR values (**Fig. 2m-n**). Consequently, the cell demonstrated impressive power densities of approximately 1.5 and 3.3 W/cm^2 at 0.7V and operating temperatures of 650 and 700 ^{o}C, respectively (**Fig. 2l**).

Nanocomposites prepared through a self-assembly process have emerged as an attractive option due to their ability to yield multi-phase catalysts with a single heat treatment at relatively low calcination temperatures[45, 46]. Generally, excessive B-site doping of Mo, W, Ce, and Zr ions into Co and Fe-based perovskites can lead to phase separation, as these elements have low solid-solution compatibility[47-50]. For instance, Shin et al. reported a self-assembled composite, composed of a B-site cation ordered double perovskite (DP) and a disordered single perovskite (SP) oxide phases, prepared by substituting W^{6+} into BSCF, resulting in $Ba_{0.5}Sr_{0.5}(Co_{0.7}Fe_{0.3})_{0.6875}W_{0.3125}O_{3-\delta}$ (BSCFW)[49]. The composite BSCFW exhibited initial and 60-hour ASR

values of 0.034 Ω cm^2 and 0.039 Ω cm^2, respectively, measured at 650 °C in static air, indicating excellent stability and comparable catalytic activity. In another development, Kim et al. introduced a superior biphasic nano-composite cathode of $Ba_{0.5}Sr_{0.5}Co_{0.6}Fe_{0.2}Zr_{0.1}Y_{0.1}O_{3-\delta}$ (BSCFZY), which self-assembles into two distinct cubic perovskites: Co-rich ($Ba_{0.5}Sr_{0.5}Co_{0.7}Fe_{0.2}Zr_{0.07}Y_{0.03}O_{3-\delta}$) and Zr-rich ($Ba_{0.6}Sr_{0.4}Co_{0.3}Fe_{0.2}Zr_{0.4}Y_{0.1}O_{3-\delta}$) phases[51]. The former promotes electrocatalytic activity, while the latter supports microstructural robustness. The synergic interplay between Co- and Zr-rich perovskite domains results in an area specific resistance of only ~0.013 Ω cm^2 at 650 °C, a considerable improvement over what would be anticipated from the individual phases. To assess the long-term stability of the BSCFZY porous cathode, the single cell underwent an extended operation of approximately 310 hours at a constant voltage load of 0.7 V and 500 °C. Remarkably, the cell displayed no discernible degradation, underscoring the exceptional stability offered by the nano-composite cathode. Moreover, in scenarios where a sudden temperature drop, possibly due to a shut-down event, or a rapid start-up for urgent power supply is required, the SOFC may experience substantial thermal stress. The prevention of cell failure in such cases critically relies on the TEC mismatch between the cathode and the electrolyte. The researchers addressed this concern by demonstrating the satisfactory thermomechanical compatibility of the BSCFZY cathode with the SDC electrolyte. They achieved this by subjecting the cell to five rapid ramping cycles, alternating between approximately 400 °C and 600 °C, with heating and cooling rates of approximately 14 °C min^{-1}. This self-assembly process led to the formation of in situ generated nanoscale interconnections with robust physical linking effects. These interconnections may help mitigate the expansion of the composite. Additionally, the residual nano-pores could serve to suppress thermal stress, thereby facilitating excellent thermomechanical compatibility with SOFC electrolytes[52, 53].

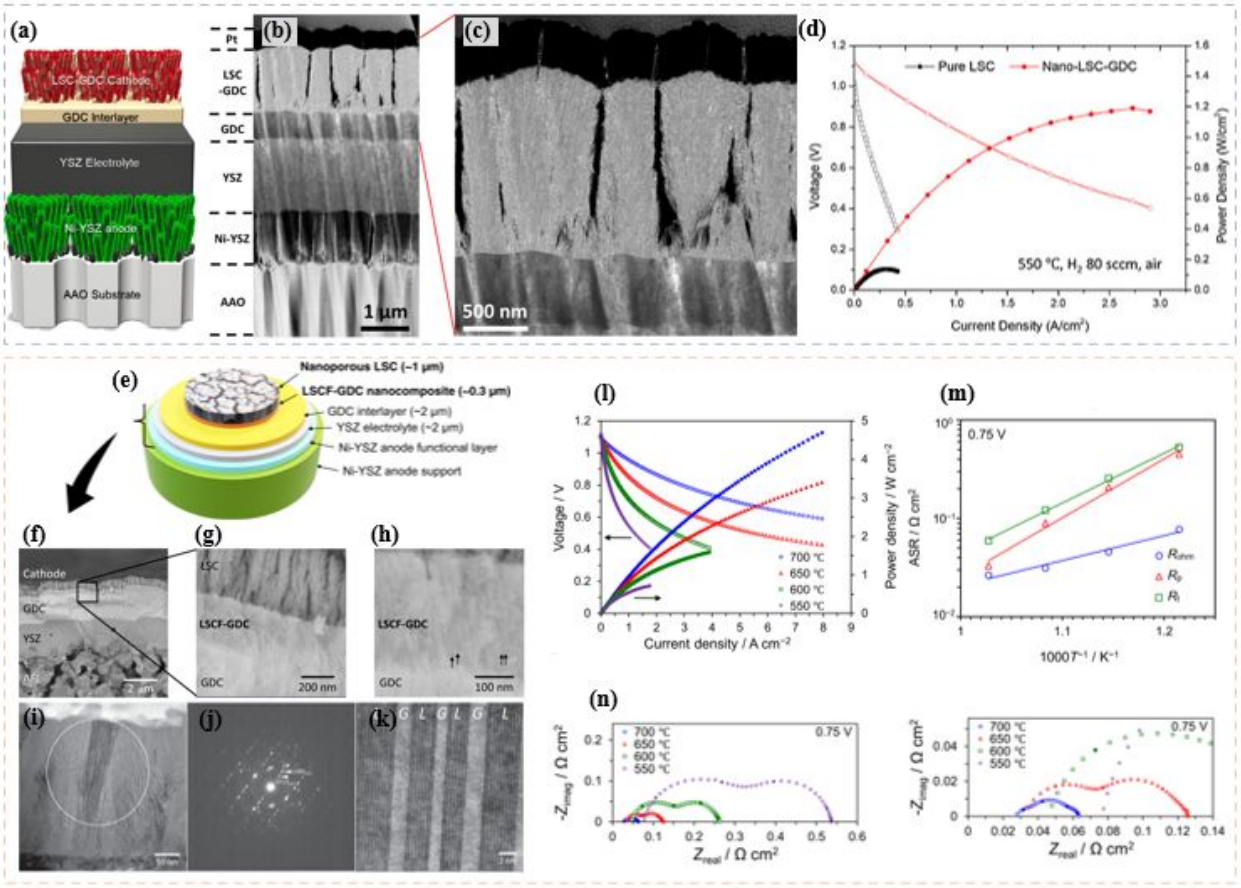

Fig. 2 (a) Configuration of TF-SOFC, (b) Dark field cross-sectional STEM image of the sputtered TF-SOFC, (c) Dark field cross-sectional STEM image of the nano-ceramic air electrode and (d) Current density vs voltage and power density characteristics for LSC-GDC/GDC/YSZ/Ni-YSZ at 550 °C[43]. Copyright 2020, ACS Appl. Energy Mater, (e) Schematic illustration of the nanoengineered cell architecture developed for the fuel electrode-supported cell, (f) Cross-sectional SEM image of the as-grown fabricated cell showing the details of the AFL, YSZ electrolyte, GDC interlayer, LSCF-GDC nanocomposite layer, and nanoporous LSC thin film, (g) High-magnification cross-sectional SEM image (the zoomed area is depicted by a square on b), (h) High-magnification cross-sectional SEM image showing details of the LSCF-GDC nanocomposite and part of the GDC interlayer, (i) Low-magnification cross-sectional TEM image depicting granular domains containing nanostrips, (j) Selected area electron diffraction (SAED) pattern of the region denoted by a circle in a, (k) STEM-HAADF lattice image of the LSCF-GDC nanocomposite film, showing the coherent, quasi-epitaxial interfaces between the LSCF and GDC phases, denoted as L and G on the image, respectively, (l) Current–voltage (I–V) and current–power (I–P) curves evaluated at evaluated using humidified (3% H_2O) H_2 as fuel and dry air as oxidant at various temperatures, (m) ASRs for the fuel electrode-supported cell as determined from impedance spectra, and (n) Impedance spectra for the fuel electrode-supported cell at an operating condition of 0.75 V[44]. Copyright 2021, Nature Communications.

Song et al. successfully developed a cobalt-free multi-phase nanocomposite, $Sr_{0.9}Ce_{0.1}Fe_{0.8}Ni_{0.2}O_{3-\delta}$ (SCFN2), as an air electrode for IT-SOFCs[46]. This composite electrode consisted of a perovskite main phase, an RP second phase, and nanosized NiO and CeO_2 minor phases. These components were intimately mixed at the nanodomain, with the NiO and CeO_2 phases mainly decorating the surface of the major phases (perovskite phase and RP phase). An SDC electrolyte-based SOFC with the SCFN2 air electrode achieved

a high PPD of 1208 mW cm^{-2} at 650 °C. Furthermore, the fuel cell with this nanocomposite electrode exhibited excellent operational stability, with no obvious degradation observed over 560 hours at 500 °C. The electrochemical performance of the SCFN2 composite surpassed that of most cobalt-free air electrodes reported thus far and was comparable to well-known cobalt-based air electrodes such as BSCF and $BaCo_{0.4}Fe_{0.4}Zr_{0.1}Y_{0.1}O_{3-\delta}$ (BCFZY) single-phase perovskite-type air electrodes.

2.2.2 Nanocomposite for proton-conducting system

PCFCs represent a category of SOFCs by using protons as charge carriers instead of oxygen ions. PCFCs offer the advantage of operating at lower temperatures due to their higher ionic conductivities and lower activation energy for proton transport. They can achieve relatively high power densities, reaching up to 0.455 $W \cdot cm^{-2}$ at 500 °C[54]. The air electrode should possess excellent conduction and exchange properties for $H^+/O^{2-}/e^-$ and remain stable under PCFC operating conditions[55-57]. By combining different phases with specific functionalities, such as bulk proton conduction, oxygen surface exchange, and triple conducting capabilities, materials with improved performance characteristics for PCFC applications are developed. In this section, we discuss the importance of designing nanocomposite materials with multiple phases to achieve enhanced performance and stability in PCFC electrodes.

Efforts have been made to introduce electronic conductivity to $BaZrO_{3-\delta}$ (BZO)/$BaCeO_{3-\delta}$-based proton conductors through the doping of rare earth metals and transition metals to turn them into electrode materials. Materials like $BaCe_{0.5}Bi_{0.5}O_{3-\delta}$, cobalt-substituted $BaZr_{0.1}Ce_{0.7}Y_{0.2}O_{3-\delta}$ (BZCY), and BZO have been synthesized, but they still exhibit insufficient conductivity for both O^{2-} and e^-, leading to limited performance[58-60]. Recent developments in high-performance intermediate-temperature reversible PCFCs have employed cobalt-based air electrodes like $PrBa_{0.5}Sr_{0.5}Co_{1.5}Fe_{0.5}O_{5+\delta}$ (PBSCF) and BCFZY[61, 62]. However, concerns remain about the thermal compatibility of these electrodes with other cell components due to their high thermal expansion coefficient[63, 64]. Researchers have also explored the concept of triple conducting oxides (TCOs), which can simultaneously transport electronic species alongside two ionic species[56, 65-68]. The approach involves combining mixed ionic and electronic conductors (MIECs) with proton conducting oxides (PCOs) or single-phase TCOs with activated catalytic species to develop nanocomposite air electrode[69](**Fig. 3**). By addressing the challenges related to air electrodes and developing suitable materials, PCFCs hold promise as a viable option for low-temperature fuel cells.

The study by Liang et al focused on the design, synthesis, and investigation of a precursor material with the nominal composition of $Ba_{0.95}(Co_{0.4}Fe_{0.4}Zr_{0.1}Y_{0.1})_{0.95}Ni_{0.05}O_{3-\delta}$ (BCFZYN-095)[70]. By manipulating the composition and cation nonstoichiometry, they were able to create a perovskite-based nanocomposite consisting of a major perovskite phase and a minor NiO phase enriched on the perovskite surface (**Fig. 3c, d**). The major perovskite phase facilitated bulk proton conduction, while the NiO nanoparticles enhanced the oxygen surface exchange process. The resulting nanocomposite exhibited a superior cathodic performance, achieving a PPD of 1040 mW cm^{-2} at 650 °C (**Fig.3e**). It also demonstrated excellent operational stability, maintaining stable performance for 400 hours at 550 °C (**Fig.3f**). The combination of bulk proton conduction and enhanced oxygen surface exchange contributed to these high-performance characteristics.

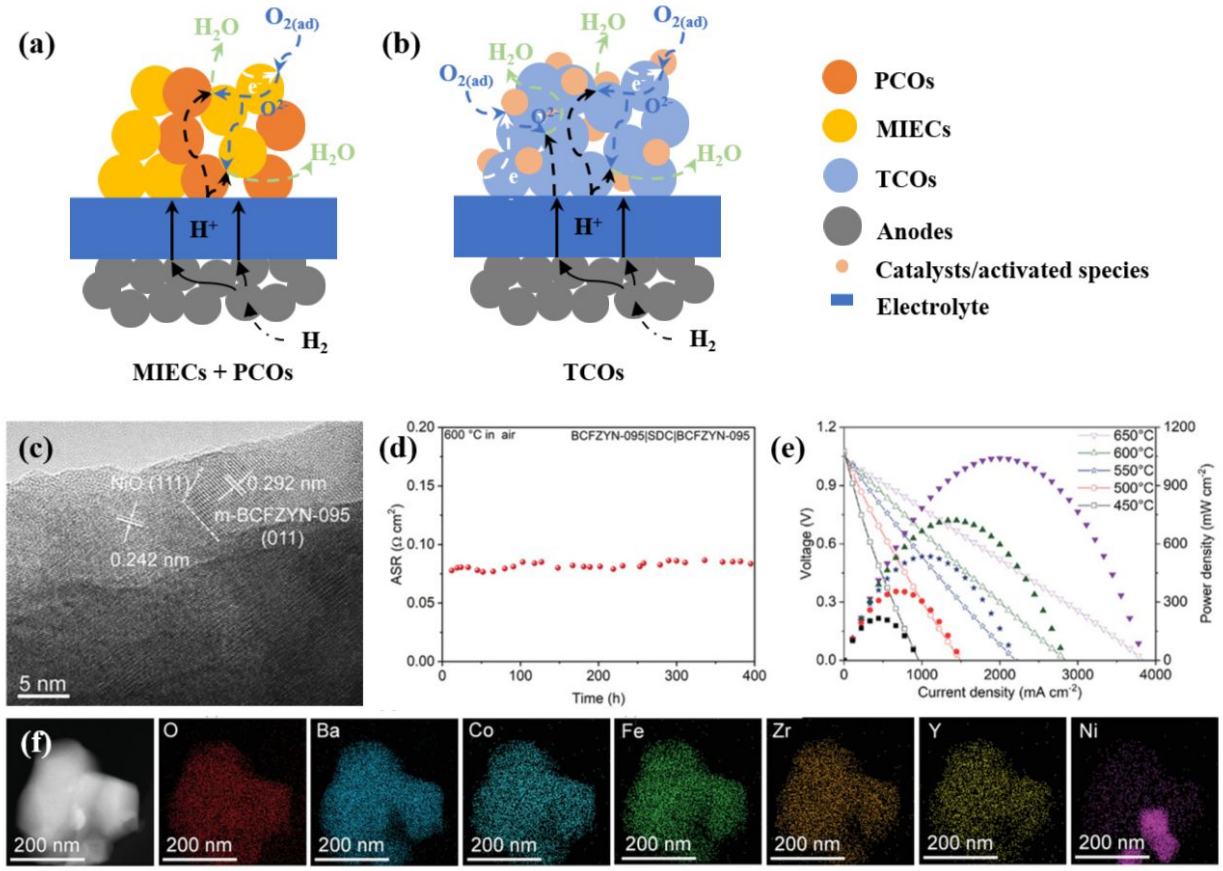

Fig. 3 Schematic illustration of electrochemical reaction mechanisms for virous electrode materials: (a) MIECs + PCOs, (b) TCOs. (c) HR-TEM image of BCFZYN-095, (d) EDX-mapping result of BCFZYN-095, (e) Time dependence of ASRs of the BCFZYN-095 electrode at 600 °C in air, based on SDC-supported symmetrical cell, (f) I–V, I–P curves and (d) impedances of the single cell with the configurations of Ni+BZCYYb|BZCYYb|BCFZYN-095 from 450 to 650 °C[70]. Copyright 2021, Advanced Materials.

In another study by Song et al, a high-performance PCFC multiphase nanocomposite air electrode was developed based on SCFN[62]. The SCFN-based electrode consisted of four phases: tetragonal $SrFeO_{3-\delta}$ (SF)-based single-phase perovskite, RP-SF-based perovskite, and CeO_2 and NiO nanoparticles enriched on the surface. When combined with a BZCYYb-1711 electrolyte, this electrode demonstrated high activity for both ORR and OER and excellent operational stability. The single cell using the SCFN air electrode achieved a high PPD of 531 mW cm^{-2} and an electrolysis current of -364 mA cm^{-2} at 1.3 V at 600 ^oC. It maintained excellent reversible stability for 120 hours at 550 °C with minimal degradation. Density functional theory (DFT) calculations suggested that the RP phase played a role in promoting hydration, proton transfer, and O^{2-} transfer, indicating fast steam/O_2 surface exchange kinetics and good $H^+/O^{2-}/e^-$ triple conducting capability. These factors contributed to the high ORR/OER activity observed in the SCFN composite.

A stable twin-phase perovskite nanocomposite of Ba-Ce-Fe-Co-O was successfully synthesized using a one-pot Pechini synthesis method. This nanocomposite consists of both cubic and orthorhombic perovskite phases and exhibited a low polarization resistance of 0.075 Ω cm_2 at 700 ^oC under an Air/H_2 gradient[71]. In another breakthrough, Liu et al. developed a novel triple-conducting bifunctional nanocomposite air electrode with exceptional performance for reversible PCFC. This achievement was made possible by combining the conventional mixed O^{2-}/e^- conductor BSCF with the BZCYYb proton conductor, employing a self-assembly one-pot synthesis method[72]. The cation exchange process between BSCF and BZCYYb further enhanced the gas (O_2/steam) surface exchange and ionic (O^{2-}/H+) bulk diffusion capabilities of the electrode. This ensured high activity for both ORR and OER. Additionally, the cation exchange within the nanocomposite electrode played a crucial role in stabilizing the crystal structure of the BSCF-based phase, reducing its thermal incompatibility with the BZCYYb-based phase in the composite air electrode. This structural stability was essential for the electrode's mechanical integrity. As a result, the reversible PCFC exhibited an impressive PPD of 1138 mW cm^{-2} at 650 ^oC under H_2/10 vol% H_2O-air operation, while maintaining excellent operational stability for 240 hours at 550 ^oC in fuel cell mode. The cell also demonstrated a high electrolysis current density of -1533 mA cm^{-2} (1.3 V) at 650 ^oC under H_2/air operation, with a durable performance over 200 hours at 550 ^oC. This achievement marks a significant advancement in the field of PCFC technology.

In addition to biphasic composites, efforts have also been made to develop multiphase nanocomposites. Song et al reported an oxygen ion-proton-electron-conducting nanocomposite, $BaCo_{0.7}(Ce_{0.8}Y_{0.2})_{0.3}O_{3-\sigma}$ (BCCY), consisted of three oxide phases of a mixed H^+/e^- conducting $BaCe_xY_yCo_zO_{3-\sigma}$ (P-BCCY) phase, mixed O^{2-}/e^- conducting $BaCo_xCe_yY_zO_{3-\sigma}$ (M-BCCY) and $BaCoO_{3-\sigma}$ (BC) phases[47]. The P-BCCY phase promotes proton diffusion, the M-BCCY phase facilitates oxygen ion diffusion, and the BC phase enhances the electronic conduction of the electrode. Additionally, the interfaces between these three phases in the nano-domain significantly increase the number of active sites for electrochemical reactions. The synergistic effect among the three phases promotes the ORR kinetics of this composite cathode and improves its thermomechanical compatibility by easing the thermal expansion coefficient mismatch.

2.3 Nanocomposites in fuel electrodes

Fuel electrodes can afford a possibility for internal reforming, high electronic conductivity, and actively catalytic partial oxidation of fuels (hydrogen, ammonia, and hydrocarbon, et.al). The reaction occurs on an oxygen ion-conducting cell and proton-conducting cell are shown as follow Eq. (1) and Eq. (2)[73], respectively:

$$H_2\,(g) + O^{2-}\,(\text{electrolyte}) \rightarrow H_2O\,(g) + 2e^-\,(\text{fuel electrode}) \quad (2)$$

$$H_2\,(g) \rightarrow 2H^+\,(\text{electrolyte}) + 2e^-\,(\text{fuel electrode}) \quad (3)$$

Nanocomposite electrodes have shown great promise in improving the kinetics of the fuel oxidation reaction (FOR) and enhancing the overall performance of fuel electrodes. This section focuses mainly on the nanoscale fuel electrodes that have been utilized in SOCs to date. The conventional Ni-cermet fuel electrodes used as the universal electrodes in SOCs for the purpose of high-temperature operation may have inevitable high polarization resistance as the temperature decreases to ~600 ^oC or lower. Thus, a finer-scale microstructure is required for SOCs operation in intermediate-temperature and low-temperature. This section covers the nano-scaled fuel electrode substrates and nanocomposite layer on the supporting structure of interest of IT-SOCs and LT-SOCs.

2.3.1 Standalone nanocomposite electrode

Integrating nanocomposite materials into fuel electrodes presents a promising avenue for enhancing their performance. These standalone nanocomposite electrodes are usually composed of a blend of materials, encompassing an ionic conductor, an electronic conductor, and a catalyst. Through precise control of the nanocomposite's composition and structure, it becomes feasible to elevate catalytic activity, amplify the

electrode-electrolyte interfacial area, and enhance fuel oxidation kinetics[74]. In this section, we provide a detailed summary of the progress in developing standalone nanocomposite fuel electrodes and delve into their performance characteristics.

Ni-YSZ is a commonly used SOCs fuel electrode material due to its high catalytic activity and electronic conductivity. However, long-term operation at high temperatures can lead to the aggregation of Ni, resulting in a decrease in the TPB area, as well as a reduction in gas diffusion due to decreased porosity[75]. To address this issue, various approaches to achieve a nanocomposite structure have been explored[76, 77]. These include the introduction of core-shell structures, infiltration of catalysts into porous fuel electrode substrates, and electrodeposition. For instance, Lim et al. synthesized core-shell structured NiO@GDC powders for use as fuel electrode substrates (**Fig. 4a-d**)[78]. The NiO cores were covered by nano-sized crystalline GDC with a spherical shape. Fuel cells fabricated using the NiO@GDC substrate exhibited significantly improved electrochemical performance compared to conventionally mixed Ni-GDC fuel electrodes. The core-shell structure of Ni@GDC, with a rigid GDC shell, effectively suppressed Ni coarsening and reduced the TPB length, resulting in improved electrochemical performance stability without significant degradation even after 500 hours of operation. Another study by Yamamoto et al. reported a NiO-GDC nanocube composite prepared using an aerosol technique with water as a green solvent (**Fig. 4e-h**)[79]. The NiO-GDC nanocubes were sintered at a relatively low temperature of 1100°C, compared to the conventional sintering temperature of 1300°C for NiO-GDC composite fuel electrode materials. This lower temperature inhibited undesirable coarsening and aggregation of NiO-GDC particles and allowed for an enlarged TPB length. The research demonstrated that GDC nanocubes with reactive (001) facets are suitable as fuel electrode materials for low-temperature SOFCs. These examples highlight the potential of nanocomposite materials in improving the performance and stability of fuel electrodes in SOFCs. The use of core-shell structures and nanocube composites offers effective strategies for mitigating the challenges associated with Ni aggregation, enhancing the electrochemical performance, and enabling operation at lower temperatures.

2.3.2 Nanocomposite on supporting structures

Utilizing nanocomposite materials in fuel electrodes through deposition on a supporting structure is another effective strategy. This approach enables optimization of the electrode microstructure and better control over the distribution and interaction of the nanocomposite components. The nanocomposite layer, comprising an ionic conductor, an electronic conductor, and a catalyst, can be deposited onto a porous

backbone, such as a ceramic or metal scaffold[80-82]. This architecture provides a high surface area for electrochemical reactions and facilitates efficient fuel delivery and gas diffusion within the electrode. By combining nanocomposite materials with a supporting structure, improved electrochemical performance, durability of the fuel electrode can be achieved.

One example of this strategy is the deposition of highly catalytically active Pd@CeO_2 nanocomposites onto porous SOFC fuel electrodes that have been functionalized with triethoxy(octyl)silane (TEOOS) (**Fig. 4i-l**)[83]. The Pd@CeO_2 nanocomposites consist of Pd nanoparticle cores coated with a porous CeO_2 shell. SOFCs with fuel electrodes modified with very low loadings (0.01 wt %) of Pd@CeO_2 nanocomposites exhibited good electrochemical performance when operated with H_2 or CH_4 fuels at 700 ^oC. Furthermore, the performance was maintained even after annealing the fuel electrode in air at 900 ^oC. In another study, Zhu et al. reported a novel hybrid catalyst composed of Ni nanoparticle-decorated $La_{0.4}Sr_{0.4}Ti_{0.9}O_{3-\delta}$ perovskite (e-LSTN) through a facile exsolution process[84]. This hybrid catalyst showed synergistic catalytic activity for the hydrogen evolution reaction (HER) in basic media. The LST component promoted water dissociation, while the Ni nanoparticles (~30 nm) enabled favorable hydrogen adsorption for recombination into H_2.

Additionally, a Ni-free ceramic fuel electrode based on a CoFe alloy (CFA) nanoparticle-decorated Ruddlesden–Popper type layered perovskite $(Pr_{0.4}Sr_{0.6})_3(Fe_{0.85}Nb_{0.15})_2O_7$ (RP-PSFN) was reported[85]. CFA nanoparticles were uniformly coated on the inner surface of the porous RP-PSFN backbone (**Fig. 4m**). This Ni-free ceramic fuel electrode demonstrated similar catalytic activity to Ni-based ceramic fuel electrodes and excellent resistance to coking. The obtained cell voltage and typical peak power densities indicate that the oxidation kinetics of C_3H_8 on the RP-PSFN-CFA fuel electrode is slower compared to H_2. This suggests that the C_3H_8 fuel oxidation reaction proceeds at a slower rate on the RP-PSFN-CFA fuel electrode compared to the hydrogen oxidation reaction. As a result, the performance of the fuel cell in terms of cell voltage and peak power density was lower when operating with C_3H_8 as the fuel compared to hydrogen. The specific values and details regarding the slower kinetics and performance differences can be found in **Fig. 4n** of the referenced study. The cell generated stable power output (0.4 A cm^{-2}) for more than 100 hours under a constant current load using wet C_3H_8 fuel at 800 °C (**Fig. 4o**), indicating effective avoidance of carbon deposition on the RP-PSFN-CFA ceramic fuel electrode (**Fig. 4p**). These examples highlight the

potential of depositing nanocomposite layers onto supporting structures to enhance the electrochemical catalytic activity and durability of fuel electrodes in SOFCs.

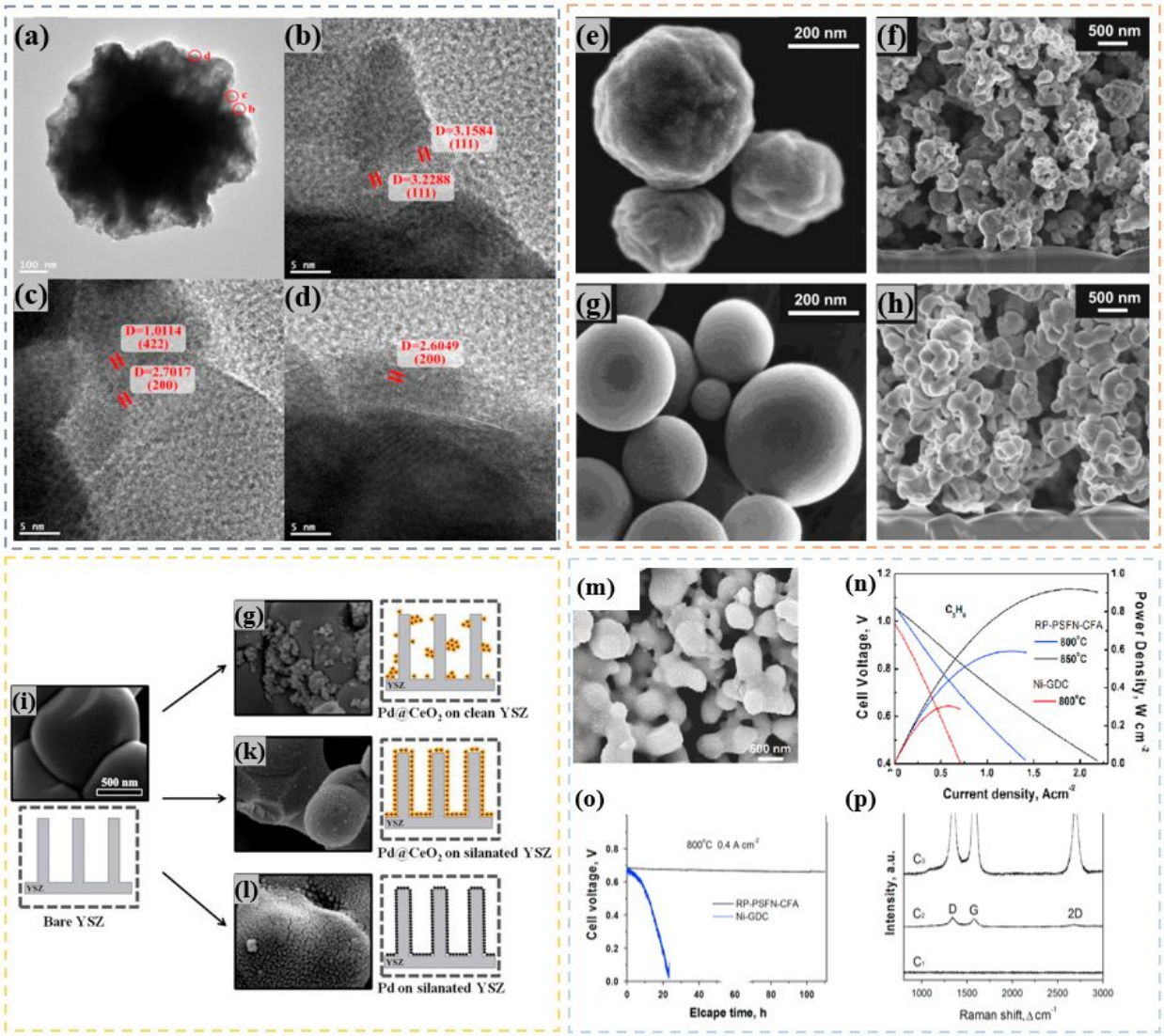

Fig. 4 (a-d) HR-TEM images of NiO@GDC particles synthesized by USP with a multi-zone furnace at pH 4 and a carrier gas flow rate of 1 L min^{-1}[78]. Copyright 2016, Ceramics International. And (e-h) (Left) SEM images of NiO–GDC composites and (Right) cross-sectional images of the NiO–GDC fuel electrode after power generation test at 600 °C: (e, f) NiO–GDC nanocube composite; (g, h) NiO–GDC composite[79]. Copyright 2014, Nano Energy. (i) SEM images along with schematic representations of the bare YSZ matrix, (g) Pd@CeO_2 nanoparticles deposited on a clean YSZ porous electrode, (k) silanated YSZ porous electrode, (l) uncoated Pd nanoparticles (2 nm) deposited on silanated YSZ porous electrode. All samples calcined at 700 °C in air, and the magnification is the same in all of the images[83]. Copyright 2013, ACS Catal. (m) SEM images of the perovskite P-PSCFN powders after reduced in H_2 at 900 °C for 2 h, (n) Current density–voltage and the corresponding power density curves of the LSGM electrolyte supported SOFCs with BCFN as air electrode and Ni-GDC or RP-PSFN-CFA composite as fuel electrode at 800 and 850 °C in wet C3H8 (~3 vol% H_2O), (o) terminal voltages measured as a function of time for the single cells operated under a constant current density of 400 mA cm^{-2} in wet C3H8 as the fuel at 800 °C. (p) Representative Raman spectra collected from RP-PSFN-CFA fuel electrode surface following the single cells operated under open circuit voltage (OCV) for 1 h (C1) and under a constant current load of 0.4 A cm^{-2} for 2 h (C2) in C3H8 fuel at 800 °C, and from the Ni-GDC

fuel electrode surface following the single cell operated under a constant current load of 0.4 A cm^{-2} for 2 h in C3H8 fuel at 800 °C (C3)[85]. Copyright 2015, Nano Energy.

The nanoparticles provide active sites for the electrochemical reactions, while the surrounding matrix facilitates charge transport to and from these sites. The proximity and interaction between the catalyst nanoparticles and the conductive matrix create favorable conditions for efficient charge transfer, leading to enhanced catalytic performance. Gan et al developed a $LaNi_{0.9}Co_{0.1}O_3$ (LNC) coated SDC composite fuel electrode synthesized by impregnation[86]. Upon reduction, LNC particles measuring 10-15 nm in size on the surface of SDC particles undergo alloy formation, resulting in a Ni-Co alloy. At a temperature of 700°C and utilizing methanol as a fuel, the single cell featuring a fuel electrode coupled with SDC-$(Li_{0.67}Na_{0.33})_2CO_3$ composite electrolyte achieved an exceptional PPD of 872 mW cm^{-2}. Compared to the conventional NiCo-SDC fuel electrode, the LNC-SDC composite fuel electrode exhibits a significantly higher catalytic activity, mainly due to the oxide supporter that impedes the aggregation of metallic nanoparticles within the LNC-SDC fuel electrode. The carbon deposition resulting from gasified methanol rises in proportion to the increase in the Ni content present in the composite fuel electrode. Moreover, cells equipped with LNC-SDC composite fuel electrodes demonstrate consistent and stable output performance over a 500-minute operational period. In addition, the core-shell structured Ni@YSZ NPs and Ag-metal oxide composite air electrodes have also been demonstrated as the thermally stable and high-performance fuel electrode materials for the high-temperature operation due to the fine Ni particle, the homogenous distribution, and the resulting increased reaction site[87, 88]. **Table 1** summarizes the state-of-the-art electrochemical performances of SOFC/SOEC where nanocomposites are used as electrodes in both oxygen and proton conducting systems.

Table 1 Summary of electrochemical performances of the most recently developed nanocomposites-based electrodes in both oxygen and proton conducting systems

Electrode properties	Nanocomposite Composition	Synthesis Method	ASR (Ω cm^2)	PPD (W cm^{-2})	Stability (h)	Ref
Fuel Electrode	NiO / $Ce_{0.8}Gd_{0.2}O_{1.9}$ (Core Shell)	Ultrasonic Spray Pyrolysis	0.002 (800 °C)	0.390 (800 °C)	500 (800 °C)	78
	NiO / GDC (Nanocube)	Aerosol Process	0.14 (600 °C)	0.067 (600 °C)	N/A	79

	$La_{0.4}Sr_{0.4}Ti_{0.9}O_{3-\delta}$ / Ni	*In-situ* Exsolution Process	N/A	N/A	N/A	84
	$(Pr_{0.4}Sr_{0.6})_3(Fe_{0.85}Nb_{0.15})_2O_7$ / CoFe alloy	*In-situ* Exsolution Process	N/A	0.930 (800 °C)	560 (800 °C)	85
	$LaNi_{0.9}Co_{0.1}O_3$ / $Ce_{0.8}Sm_{0.2}O_{1.9}$ / Ni-Co	Impregnation and Exsolution	0.1 (700 °C)	0.872 (800 °C)	N/A	86
Air Electrode	$La_{0.8}Sr_{0.2}MnO_{3-\delta}$ / $Ce_{0.8}Gd_{0.2}O_{1.9}$	Spray Pyrolysis	0.650 (vs OCV, 800 °C)	N/A	20 (800 °C)	38
	$Sm_{0.5}Sr_{0.5}CoO_{3-\delta}$ / $Ce_{0.8}Sm_{0.2}O_{1.9}$	Spray Pyrolysis	0.052 (vs OCV, 750 °C)	N/A	2000 (750 °C)	15
	$LaCoO_{3-\delta}$ / Gd-Ce alloy	Magnetron Co-sputtering	1.300 (vs OCV, 550 °C)	2.560 (600 °C)	N/A	43
	$La_{0.6}Sr_{0.4}Co_{0.2}Fe_{0.8}O_{3-\delta}$ / $Ce_{0.9}Gd_{0.1}O_{2-\delta}$	Pulsed Laser Deposition	0.030 (vs 0.75 V, 700 °C)	1.500 (650 °C)	250 (700 °C)	44
	$Ba_{0.5}Sr_{0.5}(Co_{0.7}Fe_{0.3})_{0.6875}W_{0.3125}O_{3-\delta}$ (SP / DP composite)	One-pot Self-assembly Process	0.034 (vs OC V, 650 °C)	N/A	60 (650 °C)	49
	$Ba_{0.5}Sr_{0.5}Co_{0.7}Fe_{0.2}Zr_{0.07}Y_{0.03}O_{3-\delta}$ / $Ba_{0.6}Sr_{0.4}Co_{0.3}Fe_{0.2}Zr_{0.4}Y_{0.1}O_{3-\delta}$	One-pot Self-assembly Process	0.013 (vs OC V, 650 °C)	1.100 (600 °C)	310 (500 °C)	51

$Sr_{0.9}Ce_{0.1}Fe_{0.8}Ni_{0.2}O_{3-\delta}$ (perovskite / RP / NiO and CeO_2)	One-pot Self-assembly Process	0.028 (vs OC V, 650 °C)	1.208 (650 °C)	560 (500 °C)	46
$Ba_{0.95}(Co_{0.4}Fe_{0.4}Zr_{0.1}Y_{0.1})_{0.95}Ni_{0.05}O_{3-\delta}$ / NiO	*In-situ* Exsolution Process	0.080 (vs OC V, 650 °C)	1.040 (650 °C)	400 (550 °C)	70
$SrFeO_{3-\delta}$ / RP- $SrFeO_{3-\delta}$ / NiO and CeO_2	One-pot Pechini Synthesis	0.200 (vs OC V, 600 °C)	0.531 (600 °C)	120 (550 °C)	62
$BaCe_{0.85}Fe_{0.15}O_{3-\delta}$ / $BaCe_{0.15}Fe_{0.85}O_{3-\delta}$	One-pot Pechini Synthesis	0.075 (vs OC V, 700 °C)	0.237 (600 °C)	N/A	71

3. Unique nature of nanocomposite

The application of nanocomposite electrodes in SOCs has shown remarkable achievement in overcoming critical challenges and enhancing device performance. The unique properties of nanocomposites, including enhanced catalytic activity, improved conductivity, and increased stability, have shown their potential as a gamechanger in SOCs technology. This section aims to delve deeper into the function mechanism of nanocomposite electrodes from many fundamental model studies, exploring four key aspects: tuning electronic structure for high catalytic performance, improved electronic/ionic conduction through interfaces, strain-stress and local defects arising from lattice mismatch, and the extension of the triple phase boundary. Understanding these mechanisms is essential for realizing the full transformative potential of nanocomposite electrodes in revolutionizing the performance of SOCs.

3.1 Tuning electronic structure for high catalytic performance and improved electronic/ionic conduction

A significant advantage of nanocomposite electrodes in SOCs is their inherent capacity to finely tune their electronic structure, thereby achieving remarkably high catalytic performance. The combination of perovskite oxides with noble metal nanoparticles has proven to be particularly effective in enhancing ORR kinetics[89]. Additionally, the incorporation of MIEC nanoparticles into a matrix composed of the same

material or other compatible substances has yielded nanocomposite electrodes with significantly improved performance. This enhancement can be attributed to the increased density of grain boundaries and the optimization of electronic and ionic conduction pathways within the electrodes. Several internal factors play a pivotal role in modulating oxygen activity, including the covalency of metal-oxygen bonds[90], surface reconstruction phenomena[91, 92], the net electronic charge of O^{2-} ions[93], and element doping[94], among others. Consequently, this section delves into a comprehensive discussion of how the fine-tuning of electronic structure leads to high catalytic performance and improved conductivity in nanocomposite electrodes.

Wang et al. conducted calculations to determine the differential charge densities, revealing the interfacial charge transfer phenomenon between nano-scaled noble metals and $SrCoO_3$ (**Fig. 5a**)[89]. In the case of both heterostructures (Pt and Ag) connected via Nm-O bonds, a fraction of electrons undergoes a transfer from the noble metal to the CoO_2 layer. This transfer is consistent with the weakening of the Co-O bond due to electron injection into the antibonding 2eg orbitals. It is worth noting that the higher work function of Pt, compared to Ag, results in a significantly lower net electron donation from Pt to $SrCoO_3$. However, the stronger Pt-O bond allows Pt atoms to effectively extract oxygen from oxides. Building upon computational modelling, **Fig. 5b** illustrates a noble-metal-assisted deoxygenation process, which leads to a topotactic phase transition (TPT) from the perovskite phase to the brownmillerite phase. This transition is accompanied by the formation of ordered oxygen vacancy channels (OVCs), induced by electron injection.

Nanocomposite electrodes can offer improved electronic and ionic conduction compared to conventional electrode materials. This is primarily attributed to the interfaces created between different nanoscale components within the electrode matrix. The interfaces act as pathways for charge carriers, facilitating their movement and enhancing overall conductivity. In the case of electronic conduction, the interfaces between electronic conductors and ionic conductors in nanocomposite electrodes promote efficient charge transfer. The presence of these interfaces creates a favorable environment for electron transfer between the catalytic sites and the external circuit[95]. Additionally, MIECs in nanocomposites enhance both the electronic and ionic conduction pathways, allowing for improved charge transport within the electrode. Similarly, in terms of ionic conduction, nanocomposite electrodes with well-defined interfaces between ionic conductors and electron conductors facilitate the movement of oxygen ions[96]. The enhanced ionic conduction paths enable faster oxygen diffusion and exchange between the electrode and the electrolyte, reducing the polarization losses and improving the cell performance.

Recent report has highlighted the promising oxygen exchange kinetics of hetero-interfaces between perovskite phases, specifically $(La_{1-x}Sr_x)CoO_3$ (LSC113) and $(La_{1-x}Sr_x)_2CoO_4$ (LSC214)[97]. These interfaces show potential for enhancing solid oxide fuel cell air electrodes due to their controllable and optimized embedding within vertically aligned nanocomposite (VAN) structures. To investigate the electronic structure, temperature-dependent studies were conducted on the VAN film. The energy gaps of LSC113 and LSC214 surfaces in the VAN structure were measured at various temperatures, including room temperature, 100 °C, 200 °C, 250 °C, 300 °C, and back to room temperature following cooling from 300 °C, all in 10^{-3} mbar of pure oxygen. Interestingly, the temperature dependence of the energy gap at the LSC214 surface in the VAN structure exhibited notable differences compared to LSC214 single-phase films. A closer examination, as shown in **Fig. 5c** and **d**, revealed that the electronic structure at the LSC214 surface in the VAN structure closely followed the behavior of the LSC113 phase, transitioning to a metallic-like state above 250 °C. This behavior can be attributed to the unique electronic activation in the LSC113/LSC214 multilayer (ML) structures. The injection of electrons from LSC113 to LSC214 across their interface (illustrated in **Fig. 5e**) leads to excess electrons in the lattice, resulting in oxygen vacancy defects on the transition metal oxides and subsequently reducing the surface electronegativity. Notably, the ease of oxygen vacancy formation on LSC113 contributes to raising the electron chemical potential (Fermi level) while decreasing the chemical potential of oxygen in the LSC113 phase[98]. Consequently, oxygen migrates from LSC214 to LSC113, and electrons migrate from LSC113 to LSC214[99]. This electron injection process and the creation of defect states in LSC214 cause the Fermi level to rise into the conduction band of the LSC214 phase, ultimately leading to the disappearance of the energy gap, as depicted in **Fig. 5d**. Moreover, the exchange of oxygen and electronic defects across the interfaces enables charge neutrality over the width of the grain surfaces in the VAN structure.

In summary, the investigation of the electronic structure in the VAN film has revealed intriguing interactions between the LSC113 and LSC214 phases, providing valuable insights into the oxygen and electron exchange phenomena at their interfaces. These findings hold significant promise for advancing the performance of solid oxide fuel cell air electrodes through the rational design of nanocomposite structures.

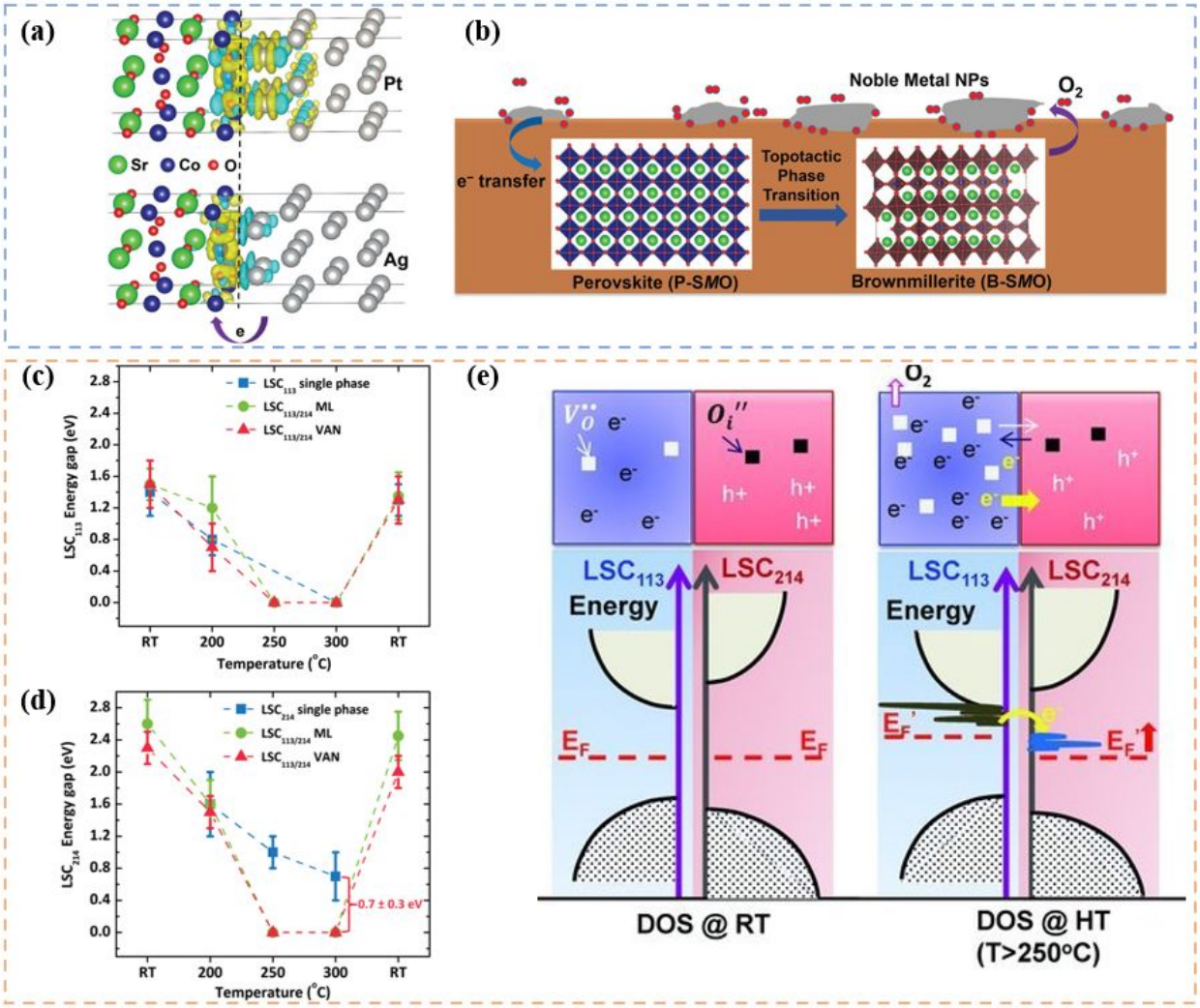

Fig. 5 (a) Charge transfer in noble metals/$SrCoO_3$ interface shown by differential charge density (isosurface value set to 0.003, cyan region denotes positive charge and yellow region denotes negative charge) and (b) Schematic diagram of deoxygenation process and topotactic phase transition (P-S*M*O to B-S*M*O) activated by noble metal nanoparticles[89]. Copyright 2021, Advanced Functional Materials. Temperature dependence of the energy gap of (c) LSC113 and (d) LSC214 in single phase, multilayer and VAN/STO structure[97]. Copyright 2015 Journal of Materials Chemistry A. Note that the surface energy gap variations with temperature in ML and VAN are quite similar for both LSC113 and LSC214 phases. The data on the multilayer system comes from ref. [99] Copyright 2013 Advanced Energy Materials and the data on the LSC113 comes from ref[96] Copyright 2014 Journal of Materials Chemistry. (e) Illustration of how the presence of reduced LSC113 surface can affect the LSC214 electronic structure through a coupling at their interface in the ML structure: upon the creation of oxygen vacancies, excess electrons in LSC113 are injected from LSC113 to LSC214. (Top) Electron injection is expected to be accompanied by the exchange of positively charged oxygen vacancies and negatively charged oxygen interstitials across the interface on the surface. (Bottom) Creation of oxygen vacancies liberates electrons and forms defect states in the energy gap, raises the Fermi level in LSC113, and thus, enables the injection of electrons into LSC214. The last step raises the Fermi level in LSC214. DOS stands for density of states; RT and HT refer to room temperature and high temperature[99]. Copyright 2013 Advanced Energy Materials.

3.2 Strain-stress/Local defects from lattice mismatch

The incorporation of different materials in nanocomposite electrodes often introduces lattice mismatch, giving rise to strain-stress effects and localized defects. In the context of SOC applications, this phenomenon can be advantageous. The strain-stress resulting from lattice mismatch has the potential to alter the electronic structure and catalytic properties of the electrode materials. Changes induced by strain in the crystal lattice, such as modified bond lengths and angles, lead to adjustments in the electronic band structure and reactivity. This strain effect can enhance catalytic activity by facilitating the adsorption and activation of reactant species, ultimately improving the electrode's performance[100]. This section provides a comprehensive summary of existing studies on the effects of lattice mismatch or in situ defects in nanocomposites on material properties.

Tsvetkov et al. have experimentally examined the effect of tensile, compressive, and no strain along the c-axis on the ORR kinetics of nanoscale $Nd_2NiO_{4+\delta}$ (NNO) thin films[101]. The corresponding strain starts were obtained by depositing NNO on (111), (110), and (100) $Y_{0.008}Zr_{0.092}O_2$ single-crystal substrates. The ORR reactivity enhancement by tensile strain and reduction by compressive strain was correlated to the increase in the concentration of oxygen interstitials (δ) and the better surface stability in the former case.

According to the analysis of the composition and microstructure of the self-assembled $BaCo_{1-x}Zr_xO_{3-\delta}$ (x = 0.8−0.2) nanocomposite developed by modified glycine nitrate process, it was concluded that the main driving force for the in-situ self-assembly of multiple phases comes from the mismatched lattice stress between different two designed dissimilar B-site ions of active cobalt and stable zirconium, which can construct a variety of perovskites with dissimilar properties of lattice structures, micro-morphologies, redox activities, thermal expansion and structural stability properties[102].

Furthermore, the lattice mismatch-induced strain can create local defects, such as dislocations or vacancies, within the nanocomposite structure. These defects can act as active sites for electrochemical reactions, promoting higher catalytic activity and facilitating charge transfer at the electrode-electrolyte interface. Additionally, the presence of these defects can enhance the ionic conduction by providing more pathways for ion transport through the electrode. A novel 3D heterostructure air electrode designed for SOFC applications is developed by incorporating LSF113 and a stoichiometric graded LSF214-based RP-material as an outer shell. The heterostructure of LSF214-LSF113 consists of LSF214 nanoislands deposited on the LSF113 substrate. The O_2 first absorbs onto the LSF113 surface and is then dissociated and incorporated with the assistance of a migrating surface oxygen vacancy. Within the LSF214-LSF113 heterostructure,

there are two parallel paths for oxygen incorporation. In Path I, the oxygen incorporation process is similar to that of pure single-phase LSF113. However, in Path II, oxygen initially adsorbs onto the LSF214 surface, dissociates, incorporates, and subsequently migrates through the LSF214 onto the LSF113 substrate. Due to the significant changes in lattice parameters between LSF113 and LSF214 (from 5.547 and 7.821 Å to 3.852 and 12.751 Å, respectively), a 31% and 63% mismatch in lattice a and c is expected, resulting in considerable tensile strain. As a consequence of this tensile strain, the kinetics of oxygen dissociation and incorporation are influenced, being limited by the availability and mobility of oxygen vacancies on the perovskite air electrode surface[103-105]. In the LSF214-LSF113 heterostructure, as the tensile strain increases, oxygen molecule adsorption and oxygen vacancy formation become more favored[104]. The increased tensile strain weakens the in-plane Fe-O bonds, leading to a more favorable formation of oxygen vacancies[105]. The strain-induced increase in available space along the oxygen migration path on LSF113 lowers the energy barrier for oxygen vacancy migration.

3.3 Extension TPB

The TPB plays a pivotal role in the performance of SOCs as it represents the region where electrochemical reactions are most actively occurring. Nanocomposite electrodes offer a remarkable extension of the TPB due to their high surface area and the presence of interfaces between different materials. This heightened surface area in nanocomposite electrodes provides a larger active interface for electrochemical reactions, resulting in improved electrode performance. Additionally, the high density of interfaces within the nanocomposite structure contributes to an increased TPB length, allowing for more efficient charge transfer and reaction kinetics. This section underscores how the extended TPB enhances the overall electrochemical activity of the electrode, leading to a more effective utilization of the electrode materials.

The TPB is a crucial factor in SOCs performance, as it represents the region where the electrochemical reactions most actively take place. Nanocomposite electrodes offer a remarkable extension of the TPB due to their high surface area and the presence of interfaces between different materials. The increased surface area of nanocomposite electrodes provides a larger active interface for the electrochemical reactions, resulting in improved electrode performance. The high density of interfaces within the nanocomposite structure contributes to a larger TPB length, enabling more efficient charge transfer and reaction kinetics. This section emphasizes the enhanced overall electrochemical activity of the electrode and promoted better utilization of the electrode materials related to the extended TPB.

As the most commonly used fuel electrode substrate, Ni-YSZ exhibits highly electronically-conductivity and compatible with the thermodynamics of the electrolyte in the ionic-conducting SOCs operated at ~800 ^{o}C. The operation mechanism of the Ni-YSZ fuel electrode has been comprehensively discussed in review by Gao et.al[106]. The transport of oxygen, hydrogen, or hydroxyl species across the interface between Ni and YSZ in SOCs is often attributed to a "spillover" mechanism. This mechanism involves the transfer of one of these species, typically on the surface, although there have been suggestions of hydrogen interstitial bulk transport as well. Among these spillover mechanisms, the hydrogen spillover mechanism (**depicted in Fig. 6a**) is widely accepted as the most prominent and recognized. Based on Butler-Volmer charge transfer kinetics, it illustrates that Ni-YSZ fuel electrode polarization depends strongly on the fuel gas composition. In addition, the fuel electrode resistance $R_{P,A}$ is more dependent on the polarization resistance as well as microstructural factors including the fuel electrode thickness L and the TPBs line length per unit electrode volume (l_{TPB}). Based on the calculation of the transmission-line model[107], Gao et al suggested that increasing l_{TPB} is a primary means for achieving low the polarization resistance of composite electrodes at low temperature. Thus, apart from adsorption, reaction, and transport processes near electrodes-electrolyte-vapor TPBs, the microstructure, particularly the density of TPB lines within the fuel electrode plays an important role in the operation of fuel electrodes. Meanwhile, combine with consideration of the relationship of YSZ/Ni particle size and l_{TPB}, the prediction of $R_{P,A}$ for a Ni-YSZ fuel electrode versus average particles size illustrates that decreasing average particle size to ~0.1 μm yields $R_{P,A} < 0.1$ Ω cm^{-2} at 600 ^{o}C, and a further decrease to ~ 0.01 μm yields $R_{P,A} < 0.1$ Ω cm^{-2} at 500 ^{o}C (**Fig. 6b**). Thus, engineering nanostructure fuel electrodes is promising for high-performance operating of SOCs in low temperature.

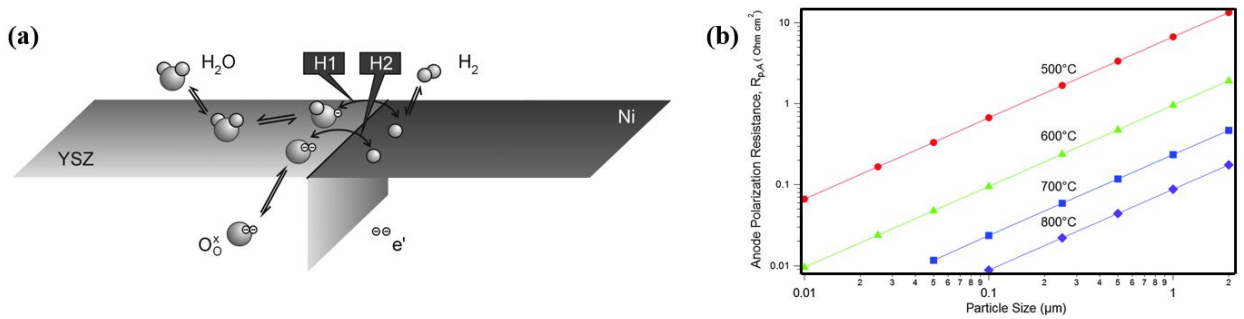

Fig. 6 (a) Schematic illustration of the hydrogen oxidation process at a Ni-YSZ TPB via the proposed "hydrogen spillover" mechanism and (b) Ni-YSZ fuel electrode polarization resistance versus feature size, assuming equal sizes for Ni and YSZ, for temperatures from 500 to 800 ^{o}C[106]. Copyright 2016, Energy & Environmental Science.

For the composite air electrodes, both electrode and electrolyte phases were pre-synthesized before forming the composite; thus, the interface between the two phases is very limited within the composites. As compared to the composite with micrometer size of the components, the building of nanocomposite will provide much enlarged activated reaction area that may bring beneficial effects for electrochemical reactions. Song et al successfully developed a cobalt-free multi-phase nanocomposite as a air electrode for IT-SOFCs[46].

4. Techniques and strategies to construct nanocomposite electrodes

Historically, composite electrodes have been prepared by simply mixing pristine materials. However, this method has its limitations, particularly in controlling the composition distribution and overall architecture of the resulting electrodes. To address this drawback, researchers have turned to synthesizing nanocomposite electrode powders using various co-sintering techniques. The synthesis process involves a meticulous selection and preparation of constituent materials to ensure the desired characteristics in the resulting nanocomposite electrodes. After synthesizing the raw nanocomposite powders, they are subsequently applied onto the electrolyte. Various methods can be utilized for this deposition process. These methods are essential to ensure proper adhesion and uniform distribution of the nanocomposite air electrode on the electrolyte surface. This section focuses on elucidating the different techniques used for preparing the raw nanocomposite powders and subsequently depositing them onto the electrolyte. The combination of appropriate preparation and deposition methods plays a critical role in producing high-performance nanocomposite air electrodes for SOCs, leading to advancements in energy conversion and storage technologies.

4.1 Preparation of the Raw Powder Precursors

Mechanical mixing: one commonly used approach for synthesizing single phase is mechanical mixing, where the constituent materials are mechanically ground or ball-milled together to achieve intimate mixing at the nanoscale. This method is relatively simple and cost-effective, making it suitable for large-scale production. Moreover, in order to be more suitable for industrial applications, the electrode preparation process should be as simple as possible, including as few steps as possible to reduce fabrication cost and time. However, it may lead to agglomeration of nanoparticles, requiring additional steps to achieve a uniform distribution[108].

One-pot Pechini method: sol-gel allows for precise control over the composition and homogeneity of the nanocomposite. By adjusting the processing parameters, such as the precursor concentration, reaction temperature, and time, the size, distribution, and composition of the nanoparticles in the nanocomposite can be tailored. Dabrowa et al reported a nano-scaled single phase perovakite-type oxides $La_{1-x}Sr_x$ (Co,Cr,Fe,Mn,Ni) $O_{3-\delta}$ (x = 0, 0.1, 0.2, 0.3, 0.4 and 0.5)[109]. However, the applicability of single-phase nanoscale materials at the industrial level is limited by the requirements of strict synthetic conditions, long reaction times, and tedious procedures. Therefore, efficient, facile, economical, and industrially feasible processing and synthesis methods for the production of nanostructured composite precursors are key to the further commercialization of SOCs technology.

Surface modification or solution method: surface modification techniques, such as surface doping or surface functionalization, can also be employed to tailor the properties of nanocomposite electrodes. Surface doping involves introducing dopant atoms onto the surface of nanoparticles to modify their electronic structure and catalytic activity[110]. Surface functionalization, on the other hand, involves the attachment of functional groups or catalyst promoters onto the nanoparticle surface to enhance reactivity and stability[111]. One strategy is the use of core-shell nanoparticles, where a catalytically active core material is coated with a protective shell. This approach provides enhanced stability by preventing the agglomeration and sintering of nanoparticles during operation[78]. Additionally, the shell material can be chosen to promote specific catalytic reactions or provide better electronic or ionic conduction properties. A Ni/YSZ fuel electrode for SOFCs was fabricated from a core–shell structured Ni/YSZ powder, which consisted of a Ni core and nano-sized YSZ shell particles[112]. The cation surfactant, cetyltrimethyl ammonium bromide (CTAB), is crucial to the synthesis of the core–shell structured Ni/YSZ powder. It was considered that CTAB was adsorbed on the surface of the negatively charged Ni and YSZ particles and served as the bridge between the Ni core and YSZ shell particles. A denser Ni/YSZ core–shell structure could be achieved when the hydrothermally synthesized 10–50 nm YSZ particles were used for the shell particles.

Spray pyrolysis: as an attractive method employed to prepare thin films, spherical and uniform ceramic powder materials for electrodes to achieve a fine microstructure, spray pyrolysis has several advantages including its open-atmosphere process, its open-reaction camber and its adjustability during deposition process, and enables control of the individual particle structure at nano-scale level, thus yielding a nano-composite powder[113]. In general, a submicron-size secondary particle (0.1-1 μm) can be formed with nano-

size crystallites (1-20 nm) by spray pyrolysis. Shimada et al devised a method for designing nanocomposite electrodes using spray pyrolysis from raw powder materials and successfully synthesized an LSM-YSZ nano-composite powder that had spherical morphology with uniform particle size using the spray pyrolysis[113]. These electrodes consisted of a perovskite oxide of SSC and a fluorite oxide of SDC and demonstrated excellent cell performance. **Fig. 7** provides a visual representation of the electrode fabrication process, emphasizing the control of the raw powder material structure to achieve high-performance nanocomposite electrodes. **Fig. 7a** illustrates the spray pyrolysis apparatus utilized in this process, involving three key steps: (i) droplet atomization, (ii) droplet transport and particle synthesis, and (iii) particle capture. **Fig. 7b** provides an illustration of a representative SSC-SDC nanocomposite particle produced through spray pyrolysis. Crystallites of SSC and SDC are uniformly dispersed within each particle. Notably, to achieve precise control over the chemical composition of the target materials during simultaneous synthesis through spray pyrolysis, it is preferable to have a minimal number of cations. Since the SSC and SDC selected for this study consist of only four cations (Co, Sr, Ce, and Sm), the SSC-SDC nanocomposite particles are highly suitable for spray pyrolysis. As shown in **Fig. 7c**, the prepared SSC-SDC nanocomposite particles were utilized to fabricate oxygen electrodes, specifically the SSC-SDC nanocomposite electrodes. The presence of nano-sized crystallites of SSC and SDC within each particle contributes to a larger surface area and an expanded TPB region within the electrodes. Additionally, during the electrode sintering process, the submicron-sized secondary particles become interconnected, forming well-connected, uniformly distributed networks of both SSC and SDC while maintaining the pore channels. The utilization of SSC-SDC nanocomposite particles, prepared through spray pyrolysis, enables precise control over the electrode structure at both the nanometer and submicrometer scales, resulting in bimodal-structured SSC-SDC nanocomposite electrodes.

In addition, the ultrasonic spray pyrolysis (USP) method is known to be a useful synthesis method based on an aerosol process for easily modification the morphology by controlling several parameters such as the solution preparation method, atomizing frequency, flow rate, and heating temperature[78]. By atomizing and turning the mixed prepared core and shell $Ni(CH_3COO)_2 \bullet 4H_2O$ and GDC precursor solutions into mists by an ultrasonic atomizer, Chae at al. successfully synthesized the core-shell structured NiO@GDC powders used as fuel electrode materials with a multi-zone furnace without post-heat treatment[78]. They investigated the influence of various parameters (i.e. the precursor pH, carrier gas flow rate, and zone

temperature) on the operation performance of the cell. The Ni@GDC synthesized in the precursor pH of 2 by USP did not exhibit any performance degradation, even after 500h. Compared to the conventionally mixed Ni-GDC fuel electrode particles, the microstructure of the Ni@GDC fuel electrode synthesized by USP showed no significant coarsening and aggregation, which effectively suppressed the decrease of TPB length.

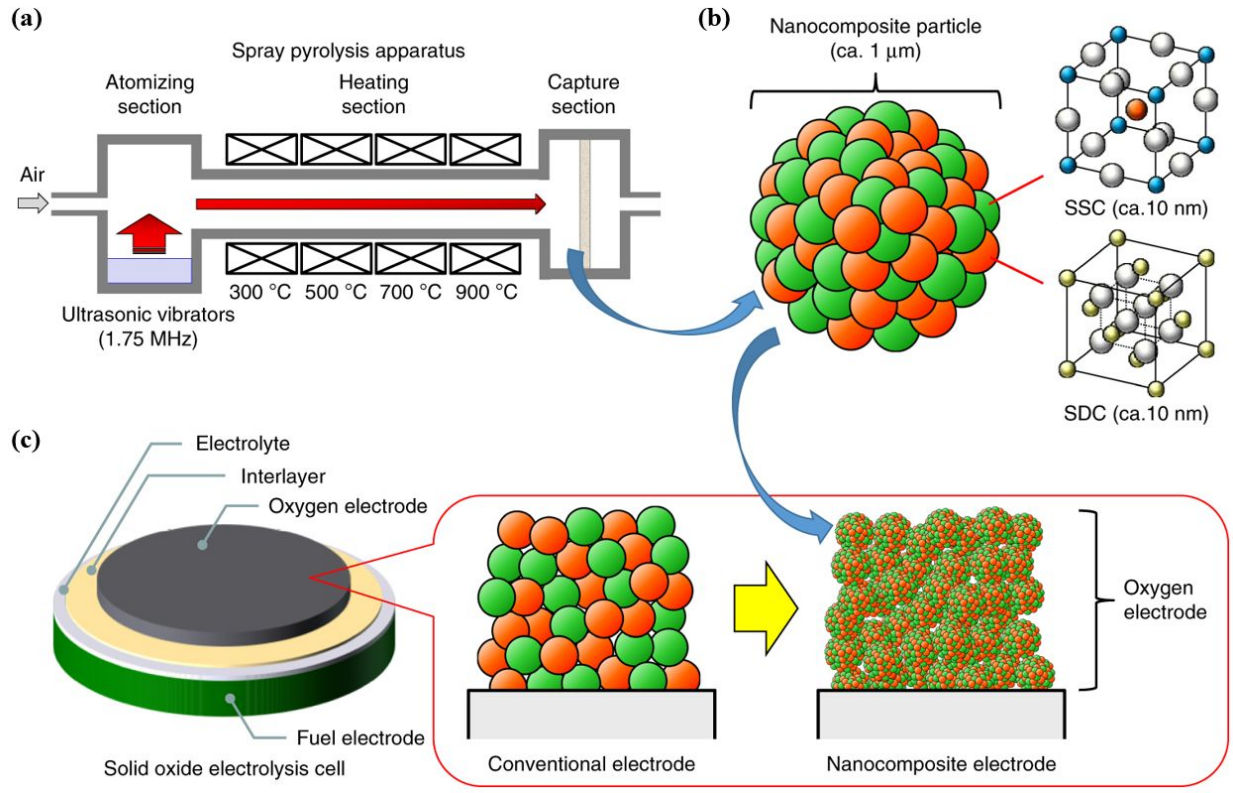

Fig. 7 Schematics of nanocomposite electrodes. (a) Spray pyrolysis apparatus consisting of atomization, heating, and capture sections, (b) Conceptual images of an SSC-SDC nanocomposite particle and (c) a bimodal-structured SSC-SDC nanocomposite electrode fabricated using the SSC-SDC nanocomposite particles[15]. Copyright 2019, Nature Communications.

4.2 Deposition Techniques

Electrode deposition techniques, including physical vapor deposition (PVD), chemical vapor deposition (CVD) and electrochemical deposition, are the versatile techniques commonly used in mass production as it can create either porous or dense films just by changing the deposition conditions[114-116]. In addition, these techniques allow for precise control over the deposition parameters, enabling the fabrication of thin films with controlled composition and morphology[116]. By selecting appropriate precursors and adjusting the deposition conditions, nanocomposite electrodes with tailored properties can be obtained.

Sputtering: a widely utilized physical vapor deposition (PVD) technique, involves bombarding a target material with ions in a vacuum environment[117, 118]. The ejected atoms condense on a substrate to form thin films. To making ceramic materials into porous films via sputtering, the most common approach is to sputter using a high pressure of sputtering gas to increase the number of collisions and decrease the kinetic energy of the deposited atoms[118]. This results in low surface mobility of the deposited atoms and the increasing effects of self-shadowing[34]. As the deposition evolves, grains are formed with well-defined and often porous grain boundaries growth in thin-film deposition[119]. In addition, atoms in the gas can form particle clusters prior to deposition aiding in the formation of porous films. If a porous ceramic electrode can be deposited through sputtering, then the entire cell can be fabricated using a single process and a single piece of equipment, which is more cost-effective and beneficial for future mass production of devices. Variations such as reactive sputtering enhance the formation of complex phases: i) reduced material particle size, thereby improving electrocatalytic activity; and ii) better adhesion of chemical bonding-based electrodes to substrates compared to ink-based deposition[108]. In nanocomposite electrode fabrication, sputtering enables precise control over film thickness and composition. The resulting uniform films exhibit good adhesion, making them suitable for SOC applications.

Pulsed Laser Deposition (PLD): utilizes a pulsed laser to ablate a target material, creating a plasma plume that deposits material onto a substrate[120-122]. This technique allows for the deposition of complex compositions and controlled nanostructures. PLD's versatility in forming epitaxial films and controlling stoichiometry is advantageous for creating high-performance nanocomposite electrodes[123]. Haowen et al successfully synthesized the self-assembled VAN nanostructure contains highly ordered alternating vertical columns of CGO and LSCO formed through a one-step thin-film deposition process that uses PLD13[42]. To obtain the nanostructured air electrode, a magnetron co-sputtering technique is employed, using Gd-Ce alloy and LSC perovskite targets. By adjusting the co-sputtering conditions, both the nanostructure and composition of the ceramic air electrode can be precisely controlled (**Fig. 8a**). In their study, 100 μm thick anodized aluminum oxide (AAO) templates with a pore size of 120 nm were utilized as the supporting substrate. The fuel electrode was fabricated by co-sputtering Ni and Y-Zr, resulting in a porous fuel electrode nanostructure with a thickness of 900 nm. Regarding the air electrode, a porous ceramic air electrode composed of LSC-GDC was deposited on the GDC interlayer using co-sputtering techniques. The thickness of the LSC-GDC air electrode ranged from 800 to 1000 nm. Lastly, a 300 nm thick Pt layer was

deposited on the air electrode to serve as a current collector. Yoon et al fabricated a complete SOFC cell by sputtering, YSZ, Ni-YSZ, and LSCF-YSZ are the materials chosen for our electrolyte, fuel electrode, and air electrode, respectively[118]. To fabricate a porous LSCF-based electrode, cosputtering of Y/Zr metal alloy and LSCF targets was performed. Since Y/Zr can be easily formed into a porous film at high Ar pressures, the cosputtering of LSCF and Y/Zr could yield a porous film of LSCF-YSZ using similar conditions (**Fig. 8b**). The resulting cosputtered LSCF-YSZ film has a porous, columnar nanostructure as shown in the SEM images in **Fig. 8c**. According to the images, this columnar structure has a diameter of tens of nanometers, thus creating a very large active surface area.

Aerosol-assisted chemical vapor deposition (AACVD): AACVD stands out in comparison to physical vapor deposition (PVD) due to its capability to generate anisotropic films that conform seamlessly to the substrate's surface. Moreover, it establishes stronger chemical bonds with the deposited layers, ensuring heightened structural integrity and functional properties[119, 124]. Serving as a derivative of traditional CVD, AACVD introduces precursor materials through aerosol droplets accompanied by carrier gases, delivering them onto a heated substrate. This strategic arrangement not only initiates the CVD reaction and film crystallization but also eliminates the necessity for a vacuum environment. As a result, the costs associated with equipment installation and maintenance are significantly diminished in comparison to conventional CVD methodologies[125]. Within the realm of AACVD, the realm of spray-Aerosol-assisted metal-organic CVD (AAMOCVD) emerges, utilizing organometallic precursors for the deposition of thin films. This technique boasts a remarkable ability to attain controlled stoichiometry, a crucial attribute when dealing with intricate oxide formation. Its proficiency in achieving these characteristics renders it particularly indispensable in the context of SOCs.

Electrochemical Vapor Deposition (EVD): EVD represents a hybrid approach merging CVD with electrochemistry. By manipulating an electric field, EVD orchestrates the precise deposition of vaporized precursors, thus enabling meticulous growth of nanocomposite electrode materials[126]. The inherent flexibility of EVD to craft tailored nanostructures on intricate geometries augments its potential for designing SOC electrodes, heralding new possibilities in this domain.

Screen Printing and Inkjet Printing: screen printing and inkjet printing hold their own as versatile means of depositing electrode materials onto substrates[127, 128]. The significance of Inkjet printing becomes particularly evident, offering meticulous control over the placement of materials and opening avenues for

fabricating intricate patterns and gradients[129]. These techniques provide a pivotal means of generating extensive-area electrodes, distinguished by their controlled compositions and morphologies.

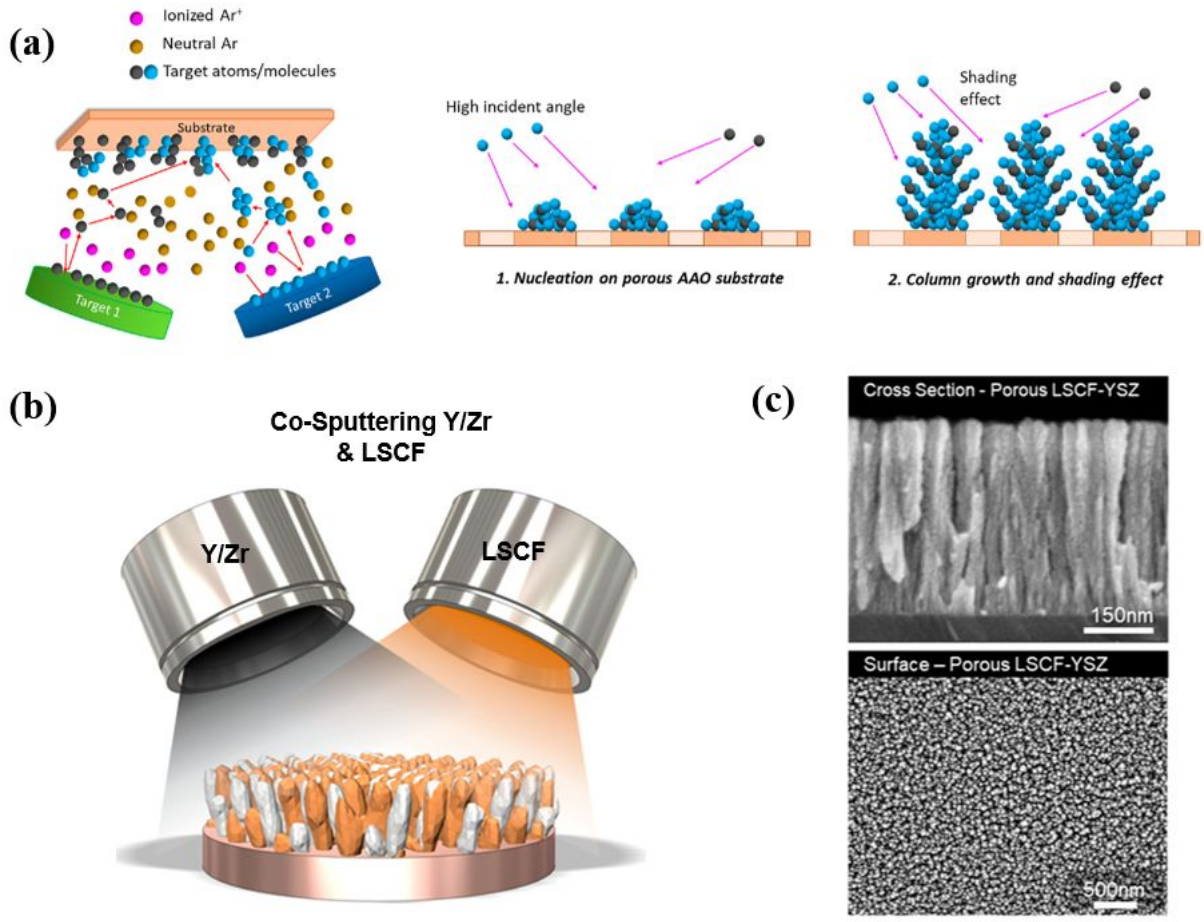

Fig. 8 (a) Schematic of the co-sputtering process and the deposited nano-ceramic air electrode nanostructure and column growth process[42]. Copyright 2020, ACS Appl. Energy Mater. (b) Co-sputtering of Y/Zr and LSCF and the corresponding porous LSCF-YSZ cross-sectional and (c) surface SEM images. Two hundred watts was applied to the LSCF ceramic target and 50 W was applied to the Y/Zr target[118]. Copyright 2020 Nano Letters.

5. Outlook and recommendation

The field of nanocomposite electrodes has shown tremendous potential in transforming the performance of SOCs. As we delve deeper into the exploration of nanoscale engineering and material design, we foresee exciting opportunities and challenges for further advancement.

Firstly, building upon the success achieved thus far, there is a pressing need to further optimize the electrochemical properties of nanocomposite electrodes. This can be achieved by tailoring the composition, nanostructure, and surface chemistry of the electrode materials. By carefully tuning the composition of

constituent materials, such as perovskites, spinels, and transition metal catalysts, we can enhance the electrochemical activity, stability, and conductivity of the electrodes. Furthermore, exploring novel nanostructuring techniques, including controlled nanoparticle size, distribution, and interfacial design, will unlock new opportunities to tailor the performance of nanocomposite electrodes.

To gain deeper insights into the nanoscale phenomena and electrochemical processes occurring within nanocomposite electrodes, the development and utilization of advanced characterization techniques are crucial. Techniques such as in-situ microscopy, operando spectroscopy, and electrochemical impedance spectroscopy can provide real-time information on the structural changes, charge transport mechanisms, and reaction kinetics within the electrodes. Integrating these advanced techniques into the characterization toolkit will significantly advance our understanding of nanocomposite electrode behavior and guide future material design strategies. The interfaces between different materials in nanocomposite electrodes have a profound impact on their electrochemical properties. Computer modeling enables the exploration and optimization of interface structures, compositions, and atomic arrangements. By employing techniques such as density functional theory (DFT) and Monte Carlo simulations, researchers can gain insights into the interfacial phenomena, such as atomic diffusion, segregation, and interfacial reactions.

To gain deeper insights into the nanoscale phenomena and electrochemical processes occurring within nanocomposite electrodes, the development and utilization of advanced characterization techniques are crucial. Techniques such as in-situ microscopy, operando spectroscopy, and electrochemical impedance spectroscopy can provide real-time information on the structural changes, charge transport mechanisms, and reaction kinetics within the electrodes. Integrating these advanced techniques into the characterization toolkit will significantly advance our understanding of nanocomposite electrode behavior and guide future material design strategies. The interfaces between different materials in nanocomposite electrodes have a profound impact on their electrochemical properties. Computer modeling enables the exploration and optimization of interface structures, compositions, and atomic arrangements. By employing techniques such as Ab initio calculations and Monte Carlo simulations, researchers can gain insights into the interfacial phenomena, such as atomic diffusion, segregation, and interfacial reactions.

While nanocomposite electrodes have demonstrated impressive performance in laboratory-scale experiments, long-term stability and durability remain critical challenges for their practical implementation. Future research should focus on improving the structural stability and chemical compatibility of

nanocomposite electrode materials with the electrolyte and other components in SOCs. By investigating degradation mechanisms, including chemical reactions and phase transformations, we can develop strategies to mitigate their impact. In addition, this can be achieved through advanced material characterization techniques, computational modeling, and accelerated aging tests.

The successful translation of nanocomposite electrodes from the laboratory to industrial-scale applications requires scalable manufacturing processes. The emphasis should be on devising cost-effective and reliable fabrication techniques that facilitate the mass production of nanocomposite electrodes while ensuring consistent quality and performance. This endeavor may entail exploring scalable deposition methods, such as roll-to-roll processes or additive manufacturing techniques. Furthermore, seamless integration of nanocomposite electrodes into SOC systems demands meticulous consideration of their compatibility with other cell components. This necessitates the development of optimized fabrication processes and dependable joining methods to guarantee a harmonious operation of SOCs with nanocomposite electrodes. Employing multi-scale modeling approaches, such as finite element analysis and computational fluid dynamics, can enhance our understanding of system-level performance, mass transport phenomena, and thermal management. By taking into account the intricate interactions between various components, computer modeling can guide the optimization of system design, electrode-electrolyte interfaces, and SOC performance.

As this field advances, it is crucial to broaden our perspective to encompass system integration aspects and conduct techno-economic analyses. This evaluation is vital for assessing the viability and economic feasibility of employing nanocomposite electrodes in large-scale SOCs. By scrutinizing their impact on overall cell performance, system cost, and energy efficiency, valuable insights can be gained to steer future research and development efforts in the right direction. The collaborative efforts of material scientists, engineers, and economists will be pivotal in surmounting the multifaceted challenges associated with nanocomposite electrodes. Moreover, it is imperative to factor in environmental and regulatory considerations throughout the development and deployment of these electrodes. This includes conducting thorough life cycle assessments and ensuring compliance with relevant industry standards. Establishing a feedback loop for continuous monitoring of performance and reliability in real-world applications will provide valuable data for refining materials and manufacturing processes over time. Additionally, conducting pilot projects and demonstrations will be instrumental in validating the scalability, performance,

and economic viability of nanocomposite electrodes in practical SOC applications, thereby instilling confidence in their industrial implementation.

6. Summary

Nanocomposite electrodes in both air and fuel electrodes of SOCs hold immense potential for enhancing their overall performance. These electrodes exploit the synergistic effects between different nanoscale components, combining their unique properties to overcome the limitations of conventional electrode materials.

The integration of mixed ionic-electronic conductors, catalysts, and other functional materials in nanocomposite structures provides avenues for tailoring the electrode's properties to meet specific performance requirements. The development of nanocomposite electrodes has also opened up opportunities for the design of tailored electronic structures, enabling the fine-tuning of their catalytic properties. The interfaces between different nanoscale components within the electrode matrix create unique electronic and ionic conduction pathways, which further enhance the electrode's performance. Moreover, the precise control of nanocomposite composition, structure, and morphology enables the optimization of the TPB promotes higher catalytic activity and improved charge transfer kinetics at the electrode-electrolyte interface.

Nanocomposite electrodes in SOC technology represent a promising concept to address the critical issues currently faced by these energy conversion devices. By utilizing nanoscale materials and tailoring their composition and structure, nanocomposite electrodes offer improved catalytic activity, enhanced electronic and ionic conduction, strain-stress and local defect generation, and an extended triple phase boundary. The versatility and tunability of nanocomposite materials, along with various construction techniques and strategies, provide a pathway to revolutionize the performance of SOCs and pave the way for more efficient and reliable energy conversion systems.

7. Author contributions

X. Li: Investigation, Conceptualization, Writing-original draft. L. Zhou: Investigation, Writing-review & editing, Q. Li: Investigation. A. Kalu: Investigation. C. Liu: Investigation. B. Guan: Investigation. A Molouk: Investigation. X. Liu: Funding Acquisition, Project Administration. W. Li: Conceptualization, Funding Acquisition, Project Administration, Writing-review & editing.

8. Conflicts of Interest

There are no conflicts of interest to declare.

9. Acknowledgements

The authors acknowledge the West Virginia University's start-up funds and the support from the United States Agency for International Development (USAID) and the Ministry of Higher Education and Scientific Research (MHESR), under program U.S.-Egypt Science and Technology Joint Fund (Cycle 19), administered by both the National Academies of Sciences, Engineering, and Medicine (NASEM) and the Science, Technology and Innovation Funding Authority (STDF).

10. Reference

1. J. Kupecki, A. Niemczyk, S. Jagielski, R. Kluczowski, M. Kosiorek and K. Machaj, *International Journal of Hydrogen Energy*, 2022, **48**, 26436-26445.
2. Y. Jiang, F. Chen and C. Xia, *Journal of Power Sources*, 2021, **493**, 229713.
3. J. Zamudio-García, L. Caizán-Juanarena, J. M. Porras-Vázquez, E. R. Losilla and D. Marrero-López, *Journal of Power Sources*, 2022, **520**, 230852.
4. Y. Zheng, J. Wang, B. Yu, W. Zhang, J. Chen, J. Qiao and J. Zhang, *Chemical Society reviews*, 2017, **46**, 1427-1463.
5. A. Ndubuisi, S. Abouali, K. Singh and V. Thangadurai, *Journal of Materials Chemistry A*, 2022, **10**, 2196-2227.
6. E. Wachsman, T. Ishihara and J. Kilner, *MRS Bulletin*, 2014, **39**, 773-779.
7. Y. Zhou, H. Wu, T. Luo, J. Wang, Y. Shi, C. Xia, S. Wang and Z. Zhan, *Advanced Energy Materials*, 2015, **5**.
8. J. Gao, Y. Liu, Y. Gao, M. Yuan, Z. Wang, Z. Lü, Q. Li and B. Wei, *Chem. Eng. J.*, 2023, **452**, 139584.
9. J. Gao, Q. Li, Z. Zhang, Z. Lü and B. Wei, *Electrochem. Commun.*, 2021, **125**, 106978.
10. S. Wang, Y. Wu, Y. Gao, H. Chen, A. M. Abdalla, A. K. Azad, Z. Lü and B. Wei, *Int. J. Hydrogen Energy*, 2022, **47**, 34205-34215.
11. P. Boldrin, E. Ruiz-Trejo, J. Mermelstein, J. M. Bermudez Menendez, T. Rami Rez Reina and N. P. Brandon, *Chem Rev*, 2016, **116**, 13633-13684.
12. Y. Shi, N. Ni, Q. Ding and X. Zhao, *Journal of Materials Chemistry A*, 2022, **10**, 2256-2270.
13. W. Li, M. Gong and X. Liu, *J. Power Sources*, 2013, **241**, 494-501.
14. W. Li, B. Guan, J. Yan, N. Zhang, X. Zhang and X. Liu, *J. Power Sources*, 2016, **318**, 178-183.
15. H. Shimada, T. Yamaguchi, H. Kishimoto, H. Sumi, Y. Yamaguchi, K. Nomura and Y. Fujishiro, *Nature communications*, 2019, **10**, 5432.
16. L. Fan, B. Zhu, P.-C. Su and C. He, *Nano Energy*, 2018, **45**, 148-176.
17. K. Chen and S. P. Jiang, *Electrochemical Energy Reviews*, 2020, **3**, 730-765.
18. Y. Yin, S. Yu, H. Dai and L. Bi, *Journal of Materials Chemistry A*, 2022, **10**, 1726-1734.
19. B. Guan, W. Li, H. Zhang and X. Liu, *J. Electrochem. Soc.*, 2015, **162**, F707-F712.
20. B. Guan, W. Li, X. Zhang and X. Liu, *ECS Trans.*, 2015, **68**, 801-808.
21. Y. Zhang, L. Shen, Y. Wang, Z. Du, B. Zhang, F. Ciucci and H. Zhao, *Journal of Materials Chemistry A*, 2022, **10**, 3495-3505.
22. Y. Tian, C. Yang, Y. Wang, M. Xu, Y. Ling, J. Pu, F. Ciucci, J. T. S. Irvine and B. Chi, *Journal of Materials Chemistry A*, 2022, **10**, 16490-16496.
23. Y. F. Sun, Y. Q. Zhang, J. Chen, J. H. Li, Y. T. Zhu, Y. M. Zeng, B. S. Amirkhiz, J. Li, B. Hua and J. L. Luo, *Nano Lett*, 2016, **16**, 5303-5309.

24. B. Hua, N. Yan, M. Li, Y. F. Sun, Y. Q. Zhang, J. Li, T. Etsell, P. Sarkar and J. L. Luo, *Advanced materials*, 2016, **28**, 8922-8926.
25. F. Dong, M. Ni, Y. Chen, D. Chen, M. O. Tadé and Z. Shao, *J. Mater. Chem. A*, 2014, **2**, 20520-20529.
26. D. Chen, C. Huang, R. Ran, H. J. Park, C. Kwak and Z. Shao, *Electrochemistry Communications*, 2011, **13**, 197-199.
27. J. Kim, Y. Choi, D.-K. Lim, J. Yoo, H. G. Seo, S. Kim, S. Kim and W. Jung, *Journal of Materials Chemistry A*, 2022, **10**, 20886-20895.
28. Z. Gao, V. Y. Zenou, D. Kennouche, L. Marks and S. A. Barnett, *Journal of Materials Chemistry A*, 2015, **3**, 9955-9964.
29. M. Forst, A. D. Caviglia, R. Scherwitzl, R. Mankowsky, P. Zubko, V. Khanna, H. Bromberger, S. B. Wilkins, Y. D. Chuang, W. S. Lee, W. F. Schlotter, J. J. Turner, G. L. Dakovski, M. P. Minitti, J. Robinson, S. R. Clark, D. Jaksch, J. M. Triscone, J. P. Hill, S. S. Dhesi and A. Cavalleri, *Nature materials*, 2015, **14**, 883-888.
30. Y. Tong, Y. Guo, P. Chen, H. Liu, M. Zhang, L. Zhang, W. Yan, W. Chu, C. Wu and Y. Xie, *Chem*, 2017, **3**, 812-821.
31. W. Li, B. Guan, T. Yang, N. Zhang, X. Zhang and X. Liu, *Phys. Chem. Chem. Phys.*, 2017, **19**, 23218-23228.
32. E. J. Crumlin, E. Mutoro, S.-J. Ahn, G. J. la O', D. N. Leonard, A. Borisevich, M. D. Biegalski, H. M. Christen and Y. Shao-Horn, *The Journal of Physical Chemistry Letters*, 2010, **1**, 3149-3155.
33. Y.-F. Sun, X.-W. Zhou, Y. Zeng, B. S. Amirkhiz, M.-N. Wang, L.-Z. Zhang, B. Hua, J. Li, J.-H. Li and J.-L. Luo, *Journal of Materials Chemistry A*, 2015, **3**, 22830-22838.
34. M. Siebenhofer, C. Riedl, A. Schmid, A. Limbeck, A. K. Opitz, J. Fleig and M. Kubicek, *J Mater Chem A Mater*, 2022, **10**, 2305-2319.
35. M. Xu, R. Cao, S. Wu, J. Lee, D. Chen and J. T. S. Irvine, *Journal of Materials Chemistry A*, 2023, **11**, 13007-13015.
36. J. S. Cronin, Y.-c. K. Chen-Wiegart, J. Wang and S. A. Barnett, *Journal of Power Sources*, 2013, **233**, 174-179.
37. C. Sun, R. Hui and J. Roller, *Journal of Solid State Electrochemistry*, 2009, **14**, 1125-1144.
38. H. Shimada, Y. Fujimaki and Y. Fujishiro, *Ceramics International*, 2020, **46**, 19617-19623.
39. D. J. Brett, A. Atkinson, N. P. Brandon and S. J. Skinner, *Chemical Society reviews*, 2008, **37**, 1568-1578.
40. A. Hagiwara, N. Hobara, K. Takizawa, K. Sato, H. Abe and M. Naito, *Solid State Ionics*, 2007, **178**, 1123-1134.
41. L. Liu, Z. Zhao, X. Zhang, D. Cui, B. Tu, D. Ou and M. Cheng, *Chem Commun (Camb)*, 2013, **49**, 777-779.
42. J. Yoon, S. Cho, J.-H. Kim, J. Lee, Z. Bi, A. Serquis, X. Zhang, A. Manthiram and H. Wang, *Advanced Functional Materials*, 2009, **19**, 3868-3873.
43. H. Ren, Y. H. Lee, E. A. Wu, H. Chung, Y. S. Meng, E. E. Fullerton and N. Q. Minh, *ACS Applied Energy Materials*, 2020, **3**, 8135-8142.
44. K. Develos-Bagarinao, T. Ishiyama, H. Kishimoto, H. Shimada and K. Yamaji, *Nature communications*, 2021, **12**, 3979.
45. Y. Chen, Y. Choi, S. Yoo, Y. Ding, R. Yan, K. Pei, C. Qu, L. Zhang, I. Chang, B. Zhao, Y. Zhang, H. Chen, Y. Chen, C. Yang, B. deGlee, R. Murphy, J. Liu and M. Liu, *Joule*, 2018, **2**, 938-949.
46. Y. Song, Y. Chen, M. Xu, W. Wang, Y. Zhang, G. Yang, R. Ran, W. Zhou and Z. Shao, *Advanced materials*, 2020, **32**, e1906979.
47. Y. Song, Y. Chen, W. Wang, C. Zhou, Y. Zhong, G. Yang, W. Zhou, M. Liu and Z. Shao, *Joule*, 2019, **3**, 2842-2853.
48. H. Qi, Z. Zhao, X. Wang, B. Tu and M. Cheng, *Ceramics International*, 2020, **46**, 22282-22289.

49. J. F. Shin, W. Xu, M. Zanella, K. Dawson, S. N. Savvin, J. B. Claridge and M. J. Rosseinsky, *Nature Energy*, 2017, **2**.
50. H. Qi, T. Zhang, D. Liu, M. Cheng and B. Tu, *Journal of Power Sources*, 2021, **506**.
51. J. H. Kim, K. Jang, D.-K. Lim, S. Ahn, D. Oh, H. Kim, J. Seo, P.-P. Choi and W. Jung, *Journal of Materials Chemistry A*, 2022, **10**, 2496-2508.
52. Y. Zhang, B. Chen, D. Guan, M. Xu, R. Ran, M. Ni, W. Zhou, R. O'Hayre and Z. Shao, *Nature*, 2021, **591**, 246-251.
53. W. A. Uju and I. N. A. Oguocha, *Materials & Design*, 2012, **33**, 503-509.
54. B. Zhu, Y. Mi, C. Xia, B. Wang, J.-S. Kim, P. Lund and T. Li, *Energy Materials*, 2021, DOI: 10.20517/energymater.2021.03.
55. W. Li, B. Guan, L. Ma, H. Tian and X. Liu, *ACS Appl. Mater. Interfaces*, 2019.
56. W. Li, B. Guan, L. Ma, S. Hu, N. Zhang and X. Liu, *J. Mater. Chem. A*, 2018, **6**, 18057-18066.
57. W. Li, B. Guan, T. Yang, Z. Li, W. Shi, H. Tian, L. Ma, T. L. Kalapos and X. Liu, *J. Power Sources*, 2021, **495**, 229764.
58. Y. Rao, S. Zhong, F. He, Z. Wang, R. Peng and Y. Lu, *International Journal of Hydrogen Energy*, 2012, **37**, 12522-12527.
59. Z. Tao, L. Bi, L. Yan, W. Sun, Z. Zhu, R. Peng and W. Liu, *Electrochem. Commun.*, 2009, **11**, 688-690.
60. L. Yang, S. Wang, X. Lou and M. Liu, *International Journal of Hydrogen Energy*, 2011, **36**, 2266-2270.
61. C. Duan, R. Kee, H. Zhu, N. Sullivan, L. Zhu, L. Bian, D. Jennings and R. O'Hayre, *Nature Energy*, 2019, **4**, 230-240.
62. Y. Song, J. Liu, Y. Wang, D. Guan, A. Seong, M. Liang, M. J. Robson, X. Xiong, Z. Zhang, G. Kim, Z. Shao and F. Ciucci, *Advanced Energy Materials*, 2021, **11**, 2101899.
63. C. Duan, D. Hook, Y. Chen, J. Tong and R. O'Hayre, *Energy & Environmental Science*, 2017, **10**, 176-182.
64. L. Jiang, T. Wei, R. Zeng, W.-X. Zhang and Y.-H. Huang, *Journal of Power Sources*, 2013, **232**, 279-285.
65. H. Ding, W. Wu, C. Jiang, Y. Ding, W. Bian, B. Hu, P. Singh, C. J. Orme, L. Wang, Y. Zhang and D. Ding, *Nature communications*, 2020, **11**, 1907.
66. N. Wang, C. Tang, L. Du, R. Zhu, L. Xing, Z. Song, B. Yuan, L. Zhao, Y. Aoki and S. Ye, *Advanced Energy Materials*, 2022, **12**, 2201882.
67. K. Pei, S. Luo, F. He, J. Arbiol, Y. Xu, F. Zhu, Y. Wang and Y. Chen, *Applied Catalysis B: Environmental*, 2023, **330**, 122601.
68. H. Zhang, K. Xu, F. He, Y. Zhou, K. Sasaki, B. Zhao, Y. Choi, M. Liu and Y. Chen, *Advanced Energy Materials*, 2022, **12**, 2200761.
69. D. Zou, Y. Yi, Y. Song, D. Guan, M. Xu, R. Ran, W. Wang, W. Zhou and Z. Shao, *Journal of Materials Chemistry A*, 2022, **10**, 5381-5390.
70. M. Liang, Y. Zhu, Y. Song, D. Guan, Z. Luo, G. Yang, S. P. Jiang, W. Zhou, R. Ran and Z. Shao, *Advanced materials*, 2022, **34**, e2106379.
71. Z. Zhao, J. Cui, M. Zou, S. Mu, H. Huang, Y. Meng, K. He, K. S. Brinkman and J. Tong, *Journal of Power Sources*, 2020, **450**.
72. Z. Liu, Y. Chen, G. Yang, M. Yang, R. Ji, Y. Song, R. Ran, W. Zhou and Z. Shao, *Applied Catalysis B: Environmental*, 2022, **319**, 121929.
73. J. A. Kilner and M. Burriel, *Annual Review of Materials Research*, 2014, **44**, 365-393.
74. T. Suzuki, Z. Hasan, Y. Funahashi, T. Yamaguchi, Y. Fujishiro and M. Awano, *Science*, 2009, **325**, 852-855.
75. V. Gonzalezdelacruz, J. Holgado, R. Pereniguez and A. Caballero, *Journal of Catalysis*, 2008, **257**, 307-314.

76. G.-Q. Shao, H. Cai, J.-R. Xie, X.-L. Duan, B.-L. Wu, R.-Z. Yuan and J.-K. Guo, *Materials Letters*, 2003, **57**, 3287-3290.
77. T. Fukui, K. Murata, S. Ohara, H. Abe, M. Naito and K. Nogi, *J. Power Sources*, 2004, **125**, 17-21.
78. C.-H. Lim and K.-T. Lee, *Ceramics International*, 2016, **42**, 13715-13722.
79. K. Yamamoto, T. Hashishin, M. Matsuda, N. Qiu, Z. Tan and S. Ohara, *Nano Energy*, 2014, **6**, 103-108.
80. M. C. Tucker, *International Journal of Hydrogen Energy*, 2020, **45**, 24203-24218.
81. R. J. Gorte and J. M. Vohs, *Current Opinion in Colloid & Interface Science*, 2009, **14**, 236-244.
82. D. Chen, M. Barreau, S. Turczyniak-Surdacka, K. Sobczak, M. Strawski, A. L. G. L. Salle, A. Efimenko, D. Teschner, C. Petit and S. Zafeiratos, *Nano Energy*, 2022, **101**.
83. L. Adijanto, A. Sampath, A. S. Yu, M. Cargnello, P. Fornasiero, R. J. Gorte and J. M. Vohs, *ACS Catalysis*, 2013, **3**, 1801-1809.
84. Y. Zhu, J. Dai, W. Zhou, Y. Zhong, H. Wang and Z. Shao, *Journal of Materials Chemistry A*, 2018, **6**, 13582-13587.
85. C. Yang, J. Li, Y. Lin, J. Liu, F. Chen and M. Liu, *Nano Energy*, 2015, **11**, 704-710.
86. T. Gan, G. Ding, X. Zhi, L. Fan, N. Hou, X. Yao, P. Li, Y. Zhao and Y. Li, *Catalysis Today*, 2019, **327**, 220-225.
87. K. Kamlungsua, T.-H. Lee, S. Lee, P.-C. Su and Y.-J. Yoon, *International Journal of Hydrogen Energy*, 2021, **46**, 30853-30860.
88. K. Kamlungsua, T.-H. Lee, S. Lee, P.-C. Su and Y.-J. Yoon, *International Journal of Hydrogen Energy*, 2021, **46**, 30853-30860.
89. Q. Wang, Y. Gu, W. Zhu, L. Han, F. Pan and C. Song, *Advanced Functional Materials*, 2021, **31**.
90. A. Grimaud, O. Diaz-Morales, B. Han, W. T. Hong, Y. L. Lee, L. Giordano, K. A. Stoerzinger, M. T. M. Koper and Y. Shao-Horn, *Nat Chem*, 2017, **9**, 457-465.
91. E. Fabbri, M. Nachtegaal, T. Binninger, X. Cheng, B. J. Kim, J. Durst, F. Bozza, T. Graule, R. Schaublin, L. Wiles, M. Pertoso, N. Danilovic, K. E. Ayers and T. J. Schmidt, *Nature materials*, 2017, **16**, 925-931.
92. A. Grimaud, A. Demortière, M. Saubanère, W. Dachraoui, M. Duchamp, M.-L. Doublet and J.-M. Tarascon, *Nature Energy*, 2016, **2**.
93. X. Wang, E. Krzystowczyk, J. Dou and F. Li, *Chemistry of Materials*, 2021, **33**, 2446-2456.
94. J. Dou, E. Krzystowczyk, X. Wang, T. Robbins, L. Ma, X. Liu and F. Li, *ChemSusChem*, 2020, **13**, 385-393.
95. C. Zhao, Y. Li, W. Zhang, Y. Zheng, X. Lou, B. Yu, J. Chen, Y. Chen, M. Liu and J. Wang, *Energy & Environmental Science*, 2020, **13**, 53-85.
96. N. Tsvetkov, Y. Chen and B. Yildiz, *Journal of Materials Chemistry A*, 2014, **2**.
97. W. Ma, J. J. Kim, N. Tsvetkov, T. Daio, Y. Kuru, Z. Cai, Y. Chen, K. Sasaki, H. L. Tuller and B. Yildiz, *Journal of Materials Chemistry A*, 2015, **3**, 207-219.
98. M. V. Ganduglia-Pirovano, A. Hofmann and J. Sauer, *Surface Science Reports*, 2007, **62**, 219-270.
99. Y. Chen, Z. Cai, Y. Kuru, W. Ma, H. L. Tuller and B. Yildiz, *Advanced Energy Materials*, 2013, **3**, 1221-1229.
100. C. Zeng, T. Adit Maark and A. A. Peterson, *The Journal of Physical Chemistry C*, 2022, **126**, 20892-20902.
101. Q. L. Nikolai Tsvetkov, Yan Chen, and Bilge Yildiz, *ACS Nano*, 2015, **9**, 1613-1621.
102. H. Qi, T. Zhang, M. Cheng, D. Liu and B. Tu, *Journal of the European Ceramic Society*, 2022, **42**, 1042-1052.
103. Y. A. Mastrikov, R. Merkle, E. Heifets, E. A. Kotomin and J. Maier, *The Journal of Physical Chemistry C*, 2010, **114**, 3017-3027.
104. S. Y. Lee, J. Yun and W.-P. Tai, *Advanced Powder Technology*, 2018, **29**, 2423-2428.

105. J. W. Han and B. Yildiz, *Energy & Environmental Science*, 2012, **5**.
106. Z. Gao, L. V. Mogni, E. C. Miller, J. G. Railsback and S. A. Barnett, *Energy & Environmental Science*, 2016, **9**, 1602-1644.
107. A. Utz, A. Leonide, A. Weber and E. Ivers-Tiffée, *Journal of Power Sources*, 2011, **196**, 7217-7224.
108. L. d. Santos-Gómez, J. Zamudio-García, J. M. Porras-Vázquez, E. R. Losilla and D. Marrero-López, *Journal of Power Sources*, 2021, **507**, 230277.
109. J. Dąbrowa, A. Olszewska, A. Falkenstein, C. Schwab, M. Szymczak, M. Zajusz, M. Moździerz, A. Mikuła, K. Zielińska, K. Berent, T. Czeppe, M. Martin and K. Świerczek, *Journal of Materials Chemistry A*, 2020, **8**, 24455-24468.
110. A. Muhulet, F. Miculescu, S. I. Voicu, F. Schütt, V. K. Thakur and Y. K. Mishra, *Materials Today Energy*, 2018, **9**, 154-186.
111. P. A. Connor, X. Yue, C. D. Savaniu, R. Price, G. Triantafyllou, M. Cassidy, G. Kerherve, D. J. Payne, R. C. Maher, L. F. Cohen, R. I. Tomov, B. A. Glowacki, R. V. Kumar and J. T. S. Irvine, *Advanced Energy Materials*, 2018, **8**, 1800120.
112. M.-J. Lee, S.-K. Hong, B.-H. Choi and H.-J. Hwang, *Ceramics International*, 2016, **42**, 10110-10115.
113. H. Shimada, T. Yamaguchi, H. Sumi, K. Nomura, Y. Yamaguchi and Y. Fujishiro, *Journal of Power Sources*, 2017, **341**, 280-284.
114. J. Leng, Z. Wang, J. Wang, H. H. Wu, G. Yan, X. Li, H. Guo, Y. Liu, Q. Zhang and Z. Guo, *Chemical Society reviews*, 2019, **48**, 3015-3072.
115. J. An, Y. B. Kim, J. Park, T. M. Gur and F. B. Prinz, *Nano Lett*, 2013, **13**, 4551-4555.
116. S. Ji, G. Y. Cho, W. Yu, P. C. Su, M. H. Lee and S. W. Cha, *ACS Appl Mater Interfaces*, 2015, **7**, 2998-3002.
117. J. Fondard, P. Bertrand, A. Billard, S. Fourcade, P. Batocchi, F. Mauvy, G. Bertrand and P. Briois, *Solid State Ionics*, 2017, **310**, 10-23.
118. Y. H. Lee, H. Ren, E. A. Wu, E. E. Fullerton, Y. S. Meng and N. Q. Minh, *Nano Lett*, 2020, **20**, 2943-2949.
119. J. W. Kim, D. Y. Jang, M. Kim, H. J. Choi and J. H. Shim, *Journal of Power Sources*, 2016, **301**, 72-77.
120. B. S. Kang, J. Matsuda, Y. W. Ju, H. H. Kim and T. Ishihara, *Nano Energy*, 2019, **56**, 382-390.
121. C.-W. Kwon, J.-W. Son, J.-H. Lee, H.-M. Kim, H.-W. Lee and K.-B. Kim, *Advanced Functional Materials*, 2011, **21**, 1154-1159.
122. Y. Zheng, Y. Li, T. Wu, W. Zhang, J. Zhu, Z. Li, J. Chen, B. Yu, J. Wang and J. Zhang, *Nano Energy*, 2018, **51**, 711-720.
123. F. Han, N. Sataa, M. Riegrafa, F. M. Fuchsb, R. Semeradc , C. Geipeld, C. Walterd and R. Costaa, *ECS Transactions*, 2019, **91**, 1157-1163.
124. D. Y. Jang, G. D. Han, H. R. Choi, M. S. Kim, H. J. Choi and J. H. Shim, *Ceramics International*, 2019, **45**, 12366-12371.
125. M. V. F. Schlupp, A. Evans, J. Martynczuk and M. Prestat, *Advanced Energy Materials*, 2014, **4**.
126. S. Z. Golkhatmi, M. I. Asghar and P. D. Lund, *Journal of Power Sources*, 2022, **552**.
127. T. Liu, J. Lin, T. Liu, H. Wu, C. Xia, C. Chen and Z. Zhan, *Journal of Electroceramics*, 2018, **40**, 138-143.
128. D. Han, J. Liu, Y.-B. He, H.-F. Wang, X.-Z. Zhang and S.-R. Wang, *International Journal of Hydrogen Energy*, 2018, **43**, 960-967.
129. J. Zhou, L. Zhang, C. Liu, J. Pu, Q. Liu, C. Zhang and S. H. Chan, *International Journal of Hydrogen Energy*, 2019, **44**, 21110-21114.